Available online at www.sciencedirect.com

SciVerse ScienceDirect

Geochimica et Cosmochimica Acta 75 (2011) 6821–6843

Geochimica et Cosmochimica Acta

www.elsevier.com/locate/gca

Group IVA irons: New constraints on the crystallization and cooling history of an asteroidal core with a complex history

T.J. McCoy [a,*], R.J. Walker [b], J.I. Goldstein [c], J. Yang [c], W.F. McDonough [b], D. Rumble [d], N.L. Chabot [e], R.D. Ash [b], C.M. Corrigan [a], J.R. Michael [f], P.G. Kotula [f]

[a] *Department of Mineral Sciences, National Museum of Natural History, Smithsonian Institution, Washington, DC 20560-0119, United States*
[b] *Department of Geology, University of Maryland, College Park, MD 20742, United States*
[c] *Department of Mechanical and Industrial Engineering, 313 Engineering Lab, University of Massachusetts, 160 Governors Drive, Amherst, MA 01003, United States*
[d] *Geophysical Laboratory, 5251 Broad Branch Road, NW, Washington, DC 20015-1305, United States*
[e] *Johns Hopkins University, Applied Physics Laboratory, 11100 Johns Hopkins Road, Laurel, MD 20723-6099, United States*
[f] *Materials Characterization Department, Sandia National Laboratories, P.O. Box 5800, MS 0886, Albuquerque, NM 87185, United States*

Received 25 May 2010; accepted in revised form 28 June 2011; available online 8 September 2011

Abstract

We report analyses of 14 group IVA iron meteorites, and the ungrouped but possibly related, Elephant Moraine (EET) 83230, for siderophile elements by laser ablation ICP-MS and isotope dilution. EET was also analyzed for oxygen isotopic composition and metallographic structure, and Fuzzy Creek, currently the IVA with the highest Ni concentration, was analyzed for metallographic structure. Highly siderophile elements (HSE) Re, Os and Ir concentrations vary by nearly three orders of magnitude over the entire range of IVA irons, while Ru, Pt and Pd vary by less than factors of five. Chondrite normalized abundances of HSE form nested patterns consistent with progressive crystal–liquid fractionation. Attempts to collectively model the HSE abundances resulting from fractional crystallization achieved best results for 3 wt.% S, compared to 0.5 or 9 wt.% S. Consistent with prior studies, concentrations of HSE and other refractory siderophile elements estimated for the bulk IVA core and its parent body are in generally chondritic proportions. Projected abundances of Pd and Au, relative to more refractory HSE, are slightly elevated and modestly differ from L/LL chondrites, which some have linked with group IVA, based on oxygen isotope similarities.

Abundance trends for the moderately volatile and siderophile element Ga cannot be adequately modeled for any S concentration, the cause of which remains enigmatic. Further, concentrations of some moderately volatile and siderophile elements indicate marked, progressive depletions in the IVA system. However, if the IVA core began crystallization with ~3 wt.% S, depletions of more volatile elements cannot be explained as a result of prior volatilization/condensation processes. The initial IVA core had an approximately chondritic Ni/Co ratio, but a fractionated Fe/Ni ratio of ~10, indicates an Fe-depleted core. This composition is most easily accounted for by assuming that the surrounding silicate shell was enriched in iron, consistent with an oxidized parent body. The depletions in Ga may reflect decreased siderophilic behavior in a relatively oxidized body, and more favorable partitioning into the silicate portion of the parent body.

Phosphate inclusions in EET show $\Delta^{17}O$ values within the range measured for silicates in IVA iron meteorites. EET has a typical ataxitic microstructure with precipitates of kamacite within a matrix of plessite. Chemical and isotopic evidence for a genetic relation between EET and group IVA is strong, but the high Ni content and the newly determined, rapid cooling rate of this meteorite show that it should continue to be classified as ungrouped. Previously reported metallographic cooling rates for IVA iron meteorites have been interpreted to indicate an inwardly crystallizing, ~150 km radius metallic body with little

* Corresponding author. Tel.: +1 202 633 2206.
E-mail address: mccoyt@si.edu (T.J. McCoy).

0016-7037/$ - see front matter Published by Elsevier Ltd.
doi:10.1016/j.gca.2011.09.006

or no silicate mantle. Hence, the IVA group was likely formed as a mass of molten metal separated from a much larger parent body that was broken apart by a large impact. Given the apparent genetic relation with IVA, EET was most likely generated via crystal–liquid fractionation in another, smaller body spawned from the same initial liquid during the impact event that generated the IVA body.
Published by Elsevier Ltd.

1. INTRODUCTION

With nearly 70 members, IVA is the third largest group of iron meteorites. IVA iron meteorites are characterized by a Widmanstätten pattern kamacite bandwidth of 0.23–0.43 mm (Buchwald, 1975), and belong to the fine octahedrite (Of) structural class. The Ni content of the group varies from ~7.45 (Jamestown) to ~12.4 (Fuzzy Creek) wt.% Ni, consistent with substantial crystal–liquid fractionation of metal in the parent body (Wasson and Richardson, 2001). The iron meteorites of this group differ from most other iron groups by their depletion in volatile siderophile elements (e.g., Ga, Ge) coupled with comparatively modest Ni contents. About half the members of the group have seen moderate to heavy shock, and a few members of the group contain silicates. It has been argued that the silicates were introduced via a high temperature impact (Wasson et al., 2006).

Almost since the recognition of the group, significant debate has ensued about their origin. Depletion in volatile siderophile elements may have been caused by pre-accretionary processes, such as nebular evaporation/condensation, acting on precursor materials (e.g., Sears, 1978). Alternately, the depletions in the IVA irons may have resulted from processes that occurred in the parent body prior to core formation, such as oxidation/reduction reactions, or impact volatilization (Wasson and Richardson, 2001; Ruzicka and Hutson, 2006; Wasson et al., 2006).

Like magmatic iron groups IIAB, IIIAB and IVB, which are generally accepted to have formed via crystal–liquid fractionation of asteroidal cores, group IVA irons exhibit element–element trends broadly consistent with fractional crystallization (Scott, 1972; Wasson and Richardson, 2001). However, although it is generally agreed that fractional crystallization played an important role, a quantitative understanding of the collective processes that led to the formation of the IVA suite remains elusive. One of the more vexing issues with respect to IVA formation is the initial S content of the system. Sulfur, and to a lesser extent P, play important roles in controlling the partitioning of siderophile elements between solid and liquid metal. Some studies have estimated that the initial S content of the IVA system was ~0.5 to 3 wt.%, based on inter-element variations of elements such as Ir–Au (Willis and Goldstein, 1982; Jones and Drake, 1983; Wasson and Richardson, 2001; Chabot, 2004; Wasson et al., 2006). Ga and Ge variations, however, cannot be easily reconciled with such low initial S. The behavior of these two volatile, moderately siderophile elements is more consistent with considerably higher initial S (e.g., ~9 wt.%; Chabot, 2004). In an attempt to develop a model that could account for all of the chemical characteristics of the IVA suite, Scott et al. (1996) considered dendritic crystallization of metal, coupled with the trapping of melt, during which S was concentrated in the liquid during fractional crystallization. This would have resulted in variable, progressive changes in the partition coefficients for siderophile elements, and could successfully account for some of the observed chemical variations. However, their model also failed to adequately account for Ga–Ge variations. Wasson and Richardson (2001) successfully modeled Ir, Au and As variations by appealing to fractional crystallization of a relatively low S system (0.5 wt.%), coupled with variable incorporation of trapped melt, but they did not rigorously consider the problematic Ga or Ge contents in their model.

The incomplete understanding of the chemical crystallization history of IVA irons is accompanied by continuing debate about the physical history of the IVA core. Numerous studies have noted the large apparent range of metallographic cooling rates among IVA irons, which is inconsistent with a slowly cooled core, mantled by appreciable silicate rock or regolith (Goldstein and Short, 1967; Rasmussen et al., 1995; Haack et al., 1996; Yang et al., 2008). The variations in cooling rates have been accounted for in several ways. For example, Haack et al. (1996) interpreted the different cooling rates to be the result of an impact-generated breakup and reassembly of a crystallizing core. The proposed scrambling and reassembly of partially differentiated metal into a new core could potentially account for the differential cooling rates, yet does not well account for the good correlation between cooling rate and extent of chemical fractionation. Wasson et al. (2006) speculated that the methodology to constrain metallographic cooling rates may be flawed, and that IVA cooling rates were actually generally constant. Yang et al. (2008) concluded that the IVA irons cooled below 650 °C at highly variable rates of 100–6600 K/Myr, where cooling rate decreased with increasing Ni content. To account for this they proposed inward crystallization of a metallic body of radius 150 ± 50 km with <1 km of silicate mantle. They determined that such a body may have formed from a differentiated protoplanet that was stripped of much of its silicate mantle via a grazing impact (e.g., Asphaug et al., 2006), and broken into several smaller bodies, one of which was molten metal with a very thin silicate mantle. Goldstein et al. (2009a,b), subsequently provided two additional cooling rate measures which support the variation of metallographic cooling rates with Ni content: cloudy taenite high-Ni particle dimensions, and tetrataenite bandwidth.

A major objective of this study is to constrain the origin and evolution of the IVA parent body from the onset of crystallization through subsolidus cooling, using both chemical trends and metallographic data. As part of this study, we also consider the possible genetic linkage between

group IVA irons and the currently ungrouped iron, Elephant Moraine (EET) 83230 (hereafter referred to as EET), an ataxite with precipitates of kamacite within a matrix of plessite, using new composition and oxygen isotope data. It has been previously suggested that EET is genetically linked to IVA, although its Ni content is much higher than any known IVA iron, and it contains large sized iron phosphates. If it is a member of chemical group IVA, it is important because it is much more chemically evolved than any other recognized IVA. Finally, in order to further consider crystallization and post-crystallization processes, we report new metallographic cooling rates for both EET and Fuzzy Creek. Fuzzy Creek is currently the IVA iron with the highest Ni content, and the only IVA sample which does not have a Widmanstätten pattern.

2. ANALYTICAL METHODS

2.1. Oxygen isotopic analysis

Phosphates from the ungrouped iron meteorite EET were analyzed for oxygen isotopes in order to examine a possible genetic relation with the IVA irons. The method of *in situ*, spot analysis for oxygen isotopes with an ultraviolet (UV) laser (Wiechert and Hoefs, 1995; Rumble et al., 1997) and purified fluorine (Asprey, 1976) was chosen in order to conserve the meteorite. Analysis of the phosphate mineral apatite for ^{16}O–^{17}O–^{18}O by *in situ* UV laser fluorination has been previously demonstrated by Jones et al. (1999), albeit with non-stoichiometric oxygen yields, and $\delta^{18}O$ values more widely dispersed than in analyses of silicate or oxide minerals by the same method. The $\delta^{17}O$ and $\delta^{18}O$ data obtained by UV laser fluorination of terrestrial apatite samples scattered parallel to and on either side of the terrestrial fraction line (TFL) (Jones et al., 1999). Despite scatter in $\delta^{18}O$ values, it is commonly observed in the analysis of oxygen isotopes that mass-dependent errors and kinetic isotope fractionation effects associated with non-stoichiometric yields of oxygen are self-canceling in relation to measured values of $\Delta^{17}O$ (Rumble et al., 2007). This is important here, as it is the $\Delta^{17}O$ that is used to assess genetic affinities.

A thin slice was cut from EET measuring approximately 1.5×1.5 cm. It contained four inclusions of Fe-phosphate 1–2 mm in diameter that were entirely surrounded by metal. The sample was placed in a reaction chamber together with polished billets of Gore Mountain garnet (USNM 107144) and San Carlos olivine (USNM 136718), evacuated, and fluorinated repeatedly with purified F_2 for 5 days until spontaneous fluorination reactions had ceased and blank O_2 was no longer measurable. Repeated pre-fluorination of samples prior to analysis by *in situ* UV laser fluorination is required to eliminate H_2O and organic contaminants absorbed along grain boundaries.

On the day of analysis, the Fe-phosphate, Gore Mountain garnet and San Carlos olivine were analyzed. The two reference materials were analyzed both before and after the analysis of EET. San Carlos olivine gave $\delta^{18}O$ and $\Delta^{17}O$ values of $+5.22 \pm 0.04‰$ and $-0.02 \pm 0.03‰$, respectively. Previous UV laser fluorination analyses for San Carlos olivine were, for USNM 136718, $\delta^{18}O = +5.23 \pm 0.15‰$, and for Harvard 131265, $\delta^{18}O = +5.19 \pm 0.08‰$, in good agreement with values obtained in the present study (Rumble et al., 1997). Gore Mountain garnet (USNM 107144) analyzed on the same day as EET phosphate gave a puzzling range of $\delta^{18}O$ values, from +5.35 to +6.20, compared to previous UV laser fluorination values of $+6.02 \pm 0.14‰$ (Rumble et al., 1997). The same analyses of Gore Mountain, however, gave the expected value of $\Delta^{17}O = +0.01 \pm 0.06‰$, so we have high confidence in the reported $\Delta^{17}O$ for EET. Both reference materials, San Carlos olivine and Gore Mountain garnet, lie on the TFL.

2.2. ^{187}Re–^{187}Os and highly siderophile element analysis of bulk samples

Pieces of 13 IVA iron meteorites were obtained from the Smithsonian Institution National Museum of Natural History (see Electronic Annex for museum sample numbers) and sawn into small chunks (0.11–0.44 g) appropriate for bulk analysis of HSE via isotope dilution (Re, Os, Ir, Ru, Pt and Pd). A piece of an additional IVA iron meteorite, Muonionalusta, was obtained from J. Blichert-Toft. EET 83230 was also obtained from the Smithsonian and analyzed as part of this analytical campaign. Prior to dissolution, each meteorite piece was mechanically cleaned by polishing with a fresh piece of carborundum, and examined using a binocular microscope to verify the absence of rust and/or inclusions.

The chemical-separation and mass spectrometric techniques used in this study for Re–Os isotopic analysis and isotope dilution analysis of Ir, Ru, Pt and Pd have been previously published (Shirey and Walker, 1995; Rehkämper et al., 1997; Cook et al., 2004; Becker et al., 2006; Walker et al., 2008). A brief description follows with additional details provided in the Electronic Annex. At least two bulk chunks of most IVA irons were analyzed. For one chunk, the polished metal, a mixed spike consisting of ^{185}Re and ^{190}Os, separate spikes consisting of ^{191}Ir, ^{104}Ru, ^{198}Pt and ^{110}Pd, approximately 6 g of concentrated HNO_3 and 3 g of concentrated HCl, were frozen into quartz or Pyrex™ Carius tubes, sealed and heated at 240 °C for more than 24 h to obtain complete sample-spike equilibration. For the second chunk, samples were processed in the same way, but only the mixed Re–Os spike and an individual ^{194}Pt spike were added in order to optimize the measurement for the ^{190}Pt–^{186}Os isotope system (not reported here). Osmium was purified using a carbon tetrachloride (CCl_4) solvent extraction technique (Cohen and Waters, 1996) follow by microdistillation purification (Birck et al., 1997). The Os total processing blank was 3 ± 2 pg ($n = 7$), and was inconsequential for all samples.

Rhenium, Ir, Ru, Pt and Pd were separated and purified from the residual acid using anion exchange columns. The Re, Ir, Ru, Pt and Pd blanks for this procedure averaged 2 ± 1, 4 ± 1, 9 ± 3, 300 ± 100 and 60 ± 20 pg, respectively, with the uncertainties defining the range ($n = 2$). All analyses are blank corrected. The blanks comprised <1% of the total element analyzed and had negligible impact on analytical uncertainties.

Osmium was analyzed via negative thermal ionization mass spectrometry (Creaser et al., 1991) using procedures previously discussed (Cook et al., 2004). For the levels of Os extracted from the IVA iron meteorites (>20 ng), external reproducibility in the $^{187}Os/^{188}Os$ ratio was ±0.05% (2σ) or better, based on repeated analyses of comparable quantities of a standard, as well as duplicate analyses (separate dissolutions of the meteorite) for all samples. For samples from which <10 ng of Os were separated for analysis (Chinautla and EET), external reproducibility in $^{187}Os/^{188}Os$ was ±0.1% (2σ)

Rhenium, Ir, Ru, Pt and Pd analyses were conducted using a *Nu Plasma* multi-collector inductively-coupled plasma mass spectrometer (MC-ICP-MS) and a *Cetac Aridus*™ desolvating nebulizer. All analyses were accomplished using static, multiple Faraday bucket collection. Salient ratios were measured to better than ±0.1% (2σ). The reported $^{187}Re/^{188}Os$ ratio 2σ uncertainties include the combined uncertainty in the isotopic measurements and blank corrections. The Os and Re blank corrections introduced maximum uncertainties of ±0.1% for all samples. The maximum analytical uncertainties in $^{187}Re/^{188}Os$ were ±0.15% for most samples. Most of the first round IVA irons were not optimally spiked for isotopic measurement. Consequently, these samples were not included in the isochron set used in the regression.

Prior studies have shown that the variance about the mean for multiple chunks of iron taken from the same piece for HSE is ⩽2% (Walker et al., 2008). This level of reproducibility includes minor variations resulting from analytical methods (weighing spikes and samples, mass spectrometric uncertainties including error magnification resulting from non-ideal spiking), as well as sample heterogeneity. Comparisons of the new data with published data are provided in the Electronic Annex Table EA1. There is considerable variability in the literature data, so the new data are in good agreement with the results of some studies, and as much as 20% different in comparison to other studies. For the modeling conducted here, relative differences in the concentrations of the HSE among IVA irons are considerably more important than absolute abundances, so systematic differences between the new and prior studies has little impact on this study.

2.3. Laser ablation ICP-MS

In situ chemical analyses of each sample analyzed for bulk HSE were conducted in order to obtain complementary bulk HSE data by another method, as well as data for a large range of other elements (including the monoisotopic HSE Rh and Au, which cannot be determined by isotope dilution). These analyses were carried out using a *Thermo-Finnigan Element 2* coupled to a laser ablation system with a photon wavelength of 213 nm (UP213, New Wave Research). The mass spectrometer was operated in a dynamic peak hopping mode with mass/charge positioning achieved by a combination of magnet current shifts and voltage offsets (Hamester et al., 1999). Details regarding the analytical system and mode of operation for iron meteorites have been recently published (Walker et al., 2008) and are only briefly reviewed here. Additional details are provided in the Electronic Annex. A comparison of the new data with published results is presented in Table EA2.

Each analysis sequence consisted of five standard reference materials (SRM) run before and after the data acquisition of three separate samples. Analyses of these SRMs provided multi-sample calibration curves used for determining element concentrations and for constraining instrument drift. The laser sampling involved the analyses of four separate, adjacent line traces (~0.8 mm long) produced using a ~100 μm diameter beam. All data were processed using the LAMTRACE (Achterbergh et al., 2001) software, which determines element concentrations based on ratios of background-subtracted count rates for samples and standards, known concentrations in the standards and the known concentration of an internal standard in the unknowns. In all cases, the internal standard for the IVA analyses was Pt, as determined by isotope dilution, and was used as an input for ^{194}Pt. Platinum is particularly useful in this role because its concentration varied little across the IVA suite. From this, concentrations of V, Cr, Mn, Cu, Zn, Ga, Ge, As, Mo, Ru, Rh, Pd, W, Re, Os, Ir and Au were determined. The detection limits used in this study were set at the background count rate plus three times the standard deviation of the background. For many elements, the standard deviation reflected spatial heterogeneities associated with trace phases, and analyses of cross-cutting taenite and kamacite bands.

Determining the magnitude of elemental heterogeneity between taenite and kamacite is important here because non-representative sampling of taenite and kamacite, in the small chunks of iron dissolved for bulk analysis of HSE, could lead to incorrect assumptions regarding the bulk compositions that are modeled. Consequently, some irons with relatively coarse taenite and kamacite were analyzed and are reported separately from the bulk in Table EA3. For some elements, differences in concentrations between the two phases were large; for other elements, differences were minor or not resolvable (Fig. EA1). Because of the likelihood of spatial overlap none of these analyses can be considered to represent pure end member compositions of either kamacite or taenite.

2.4. Metallography and cooling rates

Samples of Fuzzy Creek and EET were examined by optical microscopy and scanning electron microscopy after standard metallographic polishing. Each sample was etched with 2% nital for various times so that the cloudy zone, if present, plessite and other features would be visible in the SEM. The SEM studies were accomplished using a ZEISS Supra 55VP field emission SEM at Sandia National Laboratories. The SEM data were obtained at 5 kV in order to maximize the measurement of surface detail. Each sample was also examined for shock effects evidenced in the microstructure by optical microscopy and SEM, and the shock level was estimated. The bulk chemical compositions of Fuzzy Creek and EET were measured using an electron probe microanalyzer. Both meteorites have a fine microstructure which is representative at the sub mm level.

Multiple quantitative line scans were taken in 1–5 μm steps across the three phases in Fuzzy Creek, and the fine plessite in EET, and the Fe, Co, Ni and P contents averaged.

Thin sections of Fuzzy Creek and EET were examined using the scanning transmission electron microscope (STEM). The iron meteorite samples were thinned for the TEM using a dual beam FEI DB-235 focused ion beam (FIB)/SEM instruments at Sandia National Laboratories. The samples had a thickness of 50–100 nm and were approximately 10 μm in length and 5 μm in width. Thin sections were cut perpendicular to kamacite–taenite interfaces in EET from the polished and etched meteorite sample surface. Using this methodology, the kamacite–taenite interface is oriented perpendicular to the surface of the thin section, the ideal geometry for measuring Ni concentration gradients which are necessary for an accurate cooling rate determination. Thin sections of selected kamacite–taenite interface regions in EET and taenite regions cut at random orientations with respect to kamacite/taenite interfaces in Fuzzy Creek were analyzed using a FEI Tecnai F30ST field emission transmission – STEM at Sandia National Laboratories, operated at 300 kV. Quantitative Ni gradients in taenite 0.5–2 μm in length were measured in a direction normal to kamacite–taenite interfaces using the stored EDS X-ray scan data. The X-ray data in each pixel were converted to composition using the Cliff–Lorimer method (Cliff and Lorimer, 1975) with X-ray spatial resolution of 2–4 nm.

Samples of Fuzzy Creek and EET were also prepared for electron backscatter diffraction (EBSD) investigation. This technique allows for the identification of various phases (kamacite and taenite) and the determination of orientation relations with respect to each other. Successful application of EBSD requires that the sample surface be clean and relatively flat and free of preparation induced damage. Meteorite samples were polished using standard metallographic polishing procedures followed by a two-step vibratory polishing procedure. The first vibratory polishing was performed using 0.1 μm Al_2O_3 for 4 h followed by a second vibratory polishing step using 0.04 μm SiO_2 for 2–4 h that produces both a mechanical polishing effect, but also acts as a chemical polish, which produces very smooth surfaces. Both steps were carried out on napped cloth. This procedure produced samples that had minimal surface relief between the kamacite and taenite, and were free of specimen preparation induced damage. EBSD studies of kamacite and taenite in meteoritic metal were accomplished using a ZEISS Supra 55VP SEM outfitted with an EBSD unit from HKL Technology, with Channel 5 software. Orientation maps of fcc and bcc regions of Fuzzy Creek and EET were made using a beam voltage of 20 kV, a beam current of about 1–2 nA, and a spot size of less than 2 nm in diameter. The sample was tilted 70° from the horizontal for orientation mapping.

In order to measure the cooling rates of Fuzzy Creek and EET, information about the nucleation process of the kamacite, the nucleation temperature, the effect of impingement by adjacent kamacite plates, the Fe–Ni and Fe–Ni–P phase diagrams, and the interdiffusion coefficients which control the growth of the Widmanstätten pattern are needed (Yang et al., 2008). The Ni profile matching method (Goldstein and Ogilvie, 1965) was used to obtain a cooling rate for individual measured taenite zoning profiles. The measured Ni composition versus distance profile across taenite adjacent to a kamacite platelet is compared to Ni profiles calculated for several assumed cooling rates. A match between the observed and calculated profiles allows a cooling rate to be determined for each meteorite (Yang and Goldstein, 2006).

Table 1
Oxygen isotope analyses of phosphate in EET 83230 by ultraviolet laser fluorination.

Sample	$\Delta^{17}O$	$\delta^{17}O$	$\delta^{18}O$
Grain A, spot 1	1.147	2.1	1.81
Grain A, spot 2	1.115	0.16	−1.81
Grain D, combined 2 spots	1.138	3.68	4.82
Average values	1.134	1.98	1.61
Standard deviation	±0.017	±1.76	±3.32

3. RESULTS

3.1. Oxygen isotopes

Phosphate inclusions from EET are characterized by a wide range in $\delta^{18}O$, from −1.8‰ to +4.8‰ (Table 1). Wide variations in $\delta^{18}O$ commonly accompany non-stoichiometric yields of oxygen owing to isotope fractionation between incompletely fluorinated, oxygen-bearing reaction products. In the case of phosphates, the guilty co-reaction product of O_2 is POF_3. Oxygen isotope fractionation between O_2 and POF_3, however is mass-dependent and, thus, has little or no impact on $\Delta^{17}O$ values (Jones et al., 1999).

The analyses of iron phosphate inclusions in EET show mutually consistent values of $\Delta^{17}O$, averaging +1.134 ± 0.017‰ (1σ) (Table 1). This value is well within the range

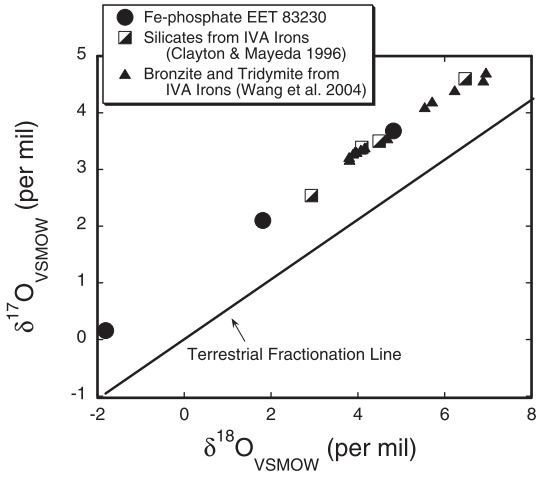

Fig. 1. Oxygen isotope data for iron phosphate inclusions in EET 83230 obtained by UV laser fluorination. Also included for comparison are data for silicates from IVA irons reported by Clayton and Mayeda (1996), and for bronzite and tridymite from IVA irons analyzed with UV laser fluorination by Wang et al. (2004).

Table 2
Osmium isotopic and HSE + Ni composition data for IVA irons. Samples are listed in order of descending Re concentration. Nickel concentrations are in wt.%, HSE are in ng/g. Δ_{187Os} – per mil deviation from isochrons.

Sample	IS	Wt. (g)	Ni	Re	Os	Ir	Ru	Pt	Pd	$^{187}Os/^{188}Os$	$^{187}Re/^{188}Os$	Δ_{187Os}
IVA irons												
Jamestown	√	0.24	74.5	379.5	4245.1	3450	4770	6648	2902	0.12939	0.4308	−0.5
	√	0.18		377.9	4229.0			6452		0.12950	0.4307	0.6
Maria Elena (1935)		0.21	75.5	348.4	3777.6	3190	4703	6621	3242	0.13011	0.4445	−4.1
	√	0.16		342.5	3762.9			6491		0.13008	0.4387	0.2
Yanhuitlan		0.19	75.1	345.9	3795.0	3193	4743	6656	3026	0.12977	0.4393	−3.3
	√	0.12		343.4	3791.9			6650		0.12978	0.4365	−1.1
La Grange		0.25	75.7	285.3	2983.1	2656	4361	6414	3430	0.13146	0.4611	−3.6
	√	0.23		284.7	3013.3			6251		0.13139	0.4554	0.1
Gibeon		0.20	77.8	272.9	2809.9	2560	4320	6088	3619	0.13215	0.4681	−2.3
	√	0.18		269.9	2797.2			6222		0.13218	0.4652	0.4
Charlotte		0.11	80.4	204.1	1954.5	1941	3862	5922	4437	0.13465	0.5036	−5.1
	√	0.21		200.2	1944.2			5787		0.13466	0.4966	0.4
Muonionalusta	√	0.24	84.8	114.5	1090.9	1146	2754	4462	6471	0.13546	0.5064	0.8
Bushman Land	√	0.24	87.6	111.0	958.55	1170	3085	5062	5663	0.13943	0.5590	−0.9
	√	0.27		112.0	966.39			4968		0.13950	0.5591	−0.3
Steinbach	√	0.33	94	71.44	542.01	783	2846	4708	6626	0.14552	0.6365	−0.9
	√	0.14		73.42	557.30			4717		0.14564	0.6362	0.5
New Westville	√	0.45	94.1	43.76	319.46	493	2047	3650	6394	0.14755	0.6617	−0.4
	√	0.25		43.62	318.29			3560		0.14760	0.6620	−0.1
Duchesne		0.44	92.8	36.32	248.77	395	1995	3193	7813	0.14882	0.6812	−2.9
	√	0.18		34.81	247.92			3222		0.14894	0.6784	0.5
		0.17		34.64	246.14			3182		0.14871	0.6800	−3.1
Duel Hill (1854)		0.44	104.5	33.70	246.36	378.9	1695	3158	7673	0.14887	0.6843	−4.9
	√	0.25		34.32	244.32			2965		0.14890	0.6788	−0.3
	√	0.23		34.33	245.04			2971		0.14889	0.6769	1.2
Fuzzy Creek		0.32	111.3	16.91	135.84	204.0	1469	2566	8142	0.14230	0.6009	−5.1
	√	0.30		16.61	133.80			2485		0.14265	0.5995	−0.5
Chinautla	√	0.29	95.4	8.605	47.662			2396		0.16423	0.8741	−0.5
		0.26		8.503	47.299	127.8	1429	2490	5207	0.16418	0.8703	2.0
EET 83230		0.21	163	8.686	63.460	95.40	1053	1616	9820	0.14643	0.6611	−11.1

of values measured in IVA iron meteorites for silicates of +1.02‰ to +1.26‰, as reported by Clayton and Mayeda (1996), and for bronzite and tridymite of +1.07‰ to +1.26‰, as reported by Wang et al. (2004) (Fig. 1).

3.2. ^{187}Re–^{187}Os and highly siderophile elements

Rhenium–Os isotopic, and bulk HSE concentration data for the IVA iron meteorites are provided in Table 2. Duplicate isotope dilution analyses of separate meteorite chunks in most instances generally provide very similar Re/Os ratios and Os isotopic compositions, within analytical uncertainties. The greatest total deviation in $^{187}Os/^{188}Os$ and $^{187}Re/^{188}Os$ from the average for duplicate or triplicate analyses of each sample was no more than 0.12% (Fuzzy Creek) and 0.89% (EET), respectively. Absolute concentrations of Re and Os in duplicate or triplicate analyses of samples varied from the average a maximum of 2.1% (Duchesne) and 1.4% (Steinbach), respectively. Duplicate or triplicate analyses of Pt also suggest reproducibility of no worse than ~±3% (for EET). Further discussion of analytical reproducibility and a comparison of data with published results are provided in the Electronic Annex Table EA1.

The new results are indicative of minimal heterogeneities with respect to HSE within bulk samples, on the mm scale sampled by different chunks. Heterogeneities resulting from the sampling of widely separated chunks of the meteorite (e.g., pieces from different museum collections) cannot be assessed here.

The moderate fractionation of Re from Os during crystallization of the IVA suite led to a range in $^{187}Re/^{188}Os$ from 0.431 (Jamestown) to 0.983 (Chinautla), and a corresponding range in $^{187}Os/^{188}Os$ from 0.1294 to 0.1642. A regression of $^{187}Os/^{188}Os$ versus $^{187}Re/^{188}Os$ data for 14 IVA irons (and five duplicate analyses) gives a slope of 0.07858 ± 0.00030 (2σ), and an initial $^{187}Os/^{188}Os = 0.09559 \pm 0.00017$ using *ISOPLOT* (Ludwig, 2003) (Fig. 2). Application of a λ for $^{187}Re = 1.666 \times 10^{-11}$ yr^{-1} (Smoliar et al., 1996) yields an age of 4540 ± 17 Ma (MSWD = 1.8). This age is significantly older than the previously reported Re–Os isochron age of 4464 ± 26 Ma, and the intercept is correspondingly lower compared with the value of 0.09584 ± 23, reported for 10 IVA iron meteorites (Smoliar et al., 1996). That study recognized considerable variance of data about the isochron they reported and eliminated data for three samples that would have been consistent with an older age. The new isochron age is similar to the Re–Os ages of other iron meteorite groups (Luck et al., 1980; Horan et al., 1992, 1998; Shen et al., 1996; Smoliar et al., 1996; Cook et al., 2004; Walker et al., 2008).

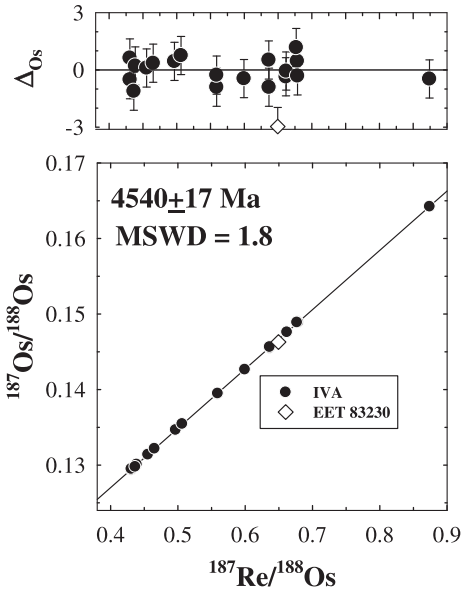

Fig. 2. $^{187}Re/^{188}Os$ versus $^{187}Os/^{188}Os$ for group IVA iron meteorites. Symbol size in lower figure is larger than analytical uncertainties. Upper diagram shows Δ values (per mil deviation of isotopic data from isochrons) versus $^{187}Re/^{188}Os$, calculated relative to the IVA isochron. Error bars represent the total analytical uncertainty (2σ) due to the isotopic measurements and the blank corrections. MSDW is the mean square weighted deviates, a measure of scatter about the regression. The currently ungrouped iron EET 83230 is shown separately.

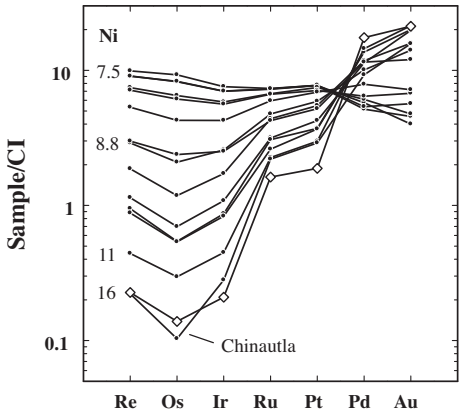

Fig. 3. CI chondrite normalized abundances of HSE for IVA irons. Elements are plotted from left to right in order of decreasing 50% condensation temperature. Data for all HSE except Au were obtained by isotope dilution analysis of bulk samples. Gold data were obtained by laser ablation ICP-MS. Normalizations were achieved using Re, Os, Ir, Ru, Pt, Pd data for the CI chondrite Orgueil from Horan et al. (2003), and Au from Anders and Grevesse (1989). For the IVA irons, Ni contents generally decrease along with Re, Os and Ru. Nickel contents (in wt.%) are shown from top to bottom for Jamestown, Bushman Land, Fuzzy Creek and EET 83230. Currently ungrouped EET 83230 is shown as the open diamond. The IVA with the lowest Os concentration, Chinautla, is highlighted for comparison.

For our suite of bulk samples, Os concentrations vary by as much as three orders of magnitude over the entire range of IVA irons, while Ru, Pt and Pd vary by less than factors of five. Chondrite normalized HSE patterns form generally nested patterns that show large variations in Re and Ir, in addition to Os (Fig. 3). The pattern shapes for evolved (high Ni) IVA irons are distinct compared to typical patterns for other magmatic iron groups (Pernicka and Wasson, 1987; Wasson, 1999; Petaev and Jacobsen, 2004; Walker et al., 2008), yet the overall trend towards greatly diminished Re, Os and Ru concentrations with increasing level of fractionation (e.g., Ni) is also present in the group IIAB and IIIAB iron meteorite suites (e.g., Cook et al., 2005). Abundances of Pd (and Au) increase with increasing level of fractionation, indicating that they were the only incompatible elements among the group of HSE measured.

Plots of Re, Os, Ru and Pt versus Ir for all IVA irons give highly-correlated linear trends (Fig. 4a). Linear regressions for all IVA data (including duplicate analyses) and associated uncertainties of these trends were calculated using the *ISOPLOT* program (Table 3). Plots of Pd, Au and Ga versus Ir do not form linear trends. Both Pd and Au versus Ir plots define curved trends (Fig. 4b). Gallium versus Ir defines an irregular trend that shows relatively little progressive change in Ga with major changes in Ir.

The Re–Os isotopic datum for EET plots slightly below the IVA isochron (Fig. 2). The HSE pattern for this iron is similar to that of Chinautla (Fig. 3), which has been previously classified as IVA, albeit anomalous because it plots well to the high Ni side of the nominal Ni versus Ga trend for IVA irons (Schaudy et al., 1972). On a plot of Ni versus Ga, EET plots along a trend with Chinautla and Fuzzy Creek, albeit much further from main IVA irons (Scott et al., 1996). On plots of Ir versus other HSE, EET plots close to the linear trends for Re, Os, Ru and Pt (Fig. 4a), yet plots above the curved IVA trends defined for Pd and Au, and well below the trend for Ga (Fig. 4b).

3.3. Bulk composition via laser ablation ICP-MS

Bulk compositional data for the IVA meteorites and EET, determined by laser ablation are reported in Table 4. Most differences between isotope dilution data for HSE, determined on relatively large bulk samples, are within analytical uncertainties of the averaged laser ablation data for each element. Minor differences outside of cited uncertainties likely reflect concentration variations on a micro scale revealed by the *in situ* analyses, compared to the averaging achieved by bulk analysis. This conclusion is supported by the minor differences that are also noted for duplicate analyses of bulk samples analyzed by isotope dilution (Table 2). Fig. 5 is a plot of the averaged element abundances in individual IVA irons, normalized to CI chondrites, with element order established by decreasing 50% condensation temperatures from left to right. While reinforcing the fractionation observed in the HSE patterns, these data also highlight the significant volatile element depletions observed in IVA irons. The refractory elements in the IVA core are in roughly chondritic proportions and, as previously observed, there is a marked and

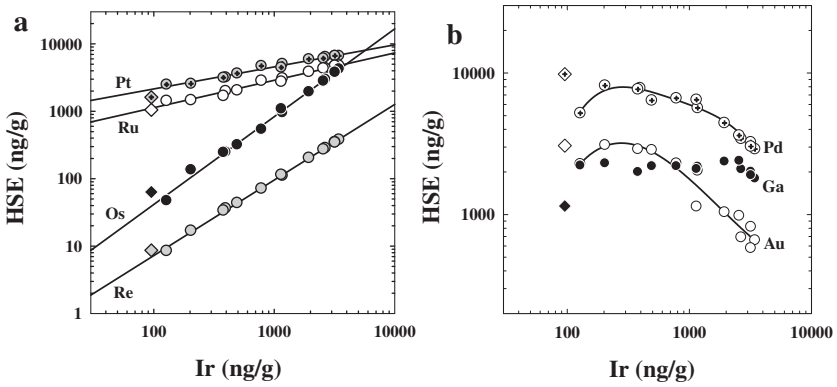

Fig. 4. Logarithmic plot of the concentration of Ir (in ng/g) versus other HSE concentrations, as well as the volatile moderately siderophile element Ga (also in ng/g). (a) Rhenium, Os, Ru and Pt data for all IVA irons plot along well-correlated linear trends. Results of regressions are provided in Table 3. (b) Palladium and Au data plot along curved arrays, consistent with D values that change in a non-linear manner relative to Ir. Gallium data show a steep increase in concentration with decrease in Ir, then a gradual decline. Data for the currently ungrouped iron EET 83230 are shown as diamonds.

Table 3
Linear regressions and uncertainties (2σ) of log–log plots of HSE concentration data versus Ir. Regressions do not include data for EET 83230. MSWD, mean squared weighted deviates.

Element	Slope	2σ	MSWD
Re	1.098	0.035	0.28
Os	1.268	0.056	3.5
Ru	0.435	0.033	1.5
Pt	0.343	0.025	1.3

progressive depletion in moderately volatile elements that follows a relative scale of half-mass condensation temperatures for a given nebular environment, with Ge being >2 orders of magnitude depleted relative to the refractory elements.

In addition to the differences in some elements between kamacite and taenite domains noted above, we also observed minor domains, as the laser beam advanced along tracks where phosphides and high Cr and Mo (oxide or phosphate?) phases were encountered; these heterogeneities reflect phases that are likely <20 μm across (with size estimate based on 3 s or less transient signals during ablation that reveal 1–2 order of magnitude sharp increases in signal intensity). Plots showing the relative partitioning of elements between kamacite (low Ni phase) and taenite (higher Ni phase) for several elements in various IVA irons are provided in the Electronic Annex Fig. EA1. Again, it is important to note that because of spatial overlap of the laser beam, end member compositions of each phase were likely rarely obtained. Important for this study is the fact that, although HSE distributions between kamacite and taenite are typically resolvable, they are not so large as to cause major biases in bulk composition data as a result of preferential sampling of one phase versus the other.

3.4. Metallography

3.4.1. Fuzzy Creek (IVA)

Fuzzy Creek has a recrystallized-reheated microstructure (Fig. 6) and lacks the expected fine octahedral structure of the IVA irons. The kamacite matrix shows a recrystallized structure with a grain size of 5–20 μm. Taenite grains, which are 2–10 μm in size are distributed on grain boundaries and kamacite triple junctions together with a smaller number of schreibersite grains (~0.5 vol %) 1–2 μm in size. Some of the taenite regions contain small kamacite precipitates while other taenite regions do not.

The bulk composition of Fuzzy Creek, obtained from line scans obtained with the electron probe microanalyzer, and accounting for the wt.% P present in small phosphides, is 12.4 wt.% Ni, 86.2 wt.% Fe, 0.49 wt.% Co and 0.18 wt.% P. Nickel and Fe contents determined by laser ablation ICP-MS are, respectively, 1.1 wt.% lower and 2.1 wt.% higher (Table 4). These differences could reflect analytical differences, or minor differences in bulk composition among different pieces of the meteorite analyzed. For the purposes here, the differences are not considered important. The average Ni content of the kamacite and phosphide phases are: 6.9 ± 0.1 and 37 wt.%, respectively. Taenite regions are not chemically homogeneous at the spatial resolution of the electron probe microanalyzer of 1 μm, and vary from 22 to 32 wt.% Ni with an average Ni content of 26.2 ± 2.8 wt.% (Yang et al., 2011).

The crystal structure of the kamacite and the taenite regions at kamacite–kamacite grain boundaries can be observed using EBSD. Fig. 7a shows the bcc kamacite grains of different orientation (color)[1] that dominate the microstructure. There is also a large amount of bcc material of differing orientation within the taenite regions at the kamacite/kamacite grain boundaries. The bcc structure is observed in the taenite regions as both bcc kamacite and as bcc martensite, α_2. The bcc martensite forms on cooling of the taenite with Ni contents less than about 28 wt.%. Fig. 7b shows the fcc taenite which has a Ni content greater than about 28 wt.% Ni. It appears from the orientation maps that there are fcc taenite regions with Ni contents above 28 wt.% and other taenite regions with fine scale

[1] For interpretation of color in this figure, the reader is referred to the web version of this article.

Table 4
Mean compositions of IVA irons determined by laser ablation ICP-MS analysis.

	Jamestown	Maria Elena (1935)	Yanhuitlan	La Grange	Gibeon	Charlotte	Bushman Land
V	0.19	0.78	0.46	0.61	0.32	0.25	–
Mn	0.56	2.3	0.52	2.3	0.74	4	0.43
Fe %	92.2	91.9	91.9	91.7	91.8	90.1	90.3
Co	3870	4230	3990	4130	3860	4955	4160
Ni %	7.5	7.7	7.7	7.9	7.8	9.4	9.3
Cu	134	149	151	148	170	175	126
Ga	1.8	2.01	1.9	2.09	2.4	2.37	2.18
Ge	0.095	0.1	0.12	0.12	0.12	0.16	0.14
As	2.3	3.03	2.5	3.8	3.8	6.2	8
Mo	4.1	5.7	4.9	5.6	4.7	6.7	6.9
Ru	4.8	5.0	4.66	4.1	4.5	4.3	3.15
Rh	0.8	0.88	0.86	0.8	0.69	0.87	0.79
Pd	2.6	2.7	2.78	2.65	3.1	3.9	5.6
W	0.7	0.52	0.7	0.51	0.6	0.57	0.46
Re	0.39	0.37	0.34	0.289	0.31	0.209	0.106
Os	4.1	3.8	3.8	3.2	2.69	1.95	0.97
Ir	3.36	3.3	3.2	2.79	2.53	2.00	1.13
Pt	6.34	6.5	6.6	6.3	6.31	5.9	5.0
Au	0.66	0.58	0.82	0.69	0.98	1.04	2.04
	Muonionalusta	Steinbach	New Westville	Duel Hill (1854)	Fuzzy Creek	Chinautla	EET 83230
V	0.2	–	–	–	0.11	–	0.3
Mn	–	0.48	0.37	0.34	0.61	2.04	0.6
Fe %	90.2	90.2	89.9	88.8	88.3	90.7	84.6
Co	3760	3895	4280	4630	4030	4095	4700
Ni %	8.4	9.4	9.7	10.8	11.3	8.9	13.6
Cu	115	131	126	137	146	131	247
Ga	2.1	2.2	2.2	2.0	2.3	2.22	1.15
Ge	–	0.14	0.15	0.14	0.13	0.18	0.069
As	–	13	12	13	15.3	14	16
Mo	7.1	6.0	7.1	6.4	4.6	7.8	2.54
Ru	3.2	2.8	2.21	1.88	1.43	1.8	1.1
Rh	0.79	0.95	0.72	0.67	0.47	0.63	0.42
Pd	6.6	5.4	6.4	7.1	6.8	6.4	7.5
W	0.37	0.51	0.34	0.30	0.24	0.39	0.54
Re	0.11	0.07	0.042	0.032	0.021	0.008	0.007
Os	1.03	0.56	0.31	0.23	0.13	0.05	0.063
Ir	1.14	0.78	0.49	0.39	0.21	0.132	0.071
Pt	3.8	4.54	3.6	3.1	2.53	2.47	0.91
Au	1.74	2.3	2.86	2.9	3.1	2.28	3.1

– Concentration data are below detection limit.
See Electronic Annex for standard deviation values of analyzed samples.

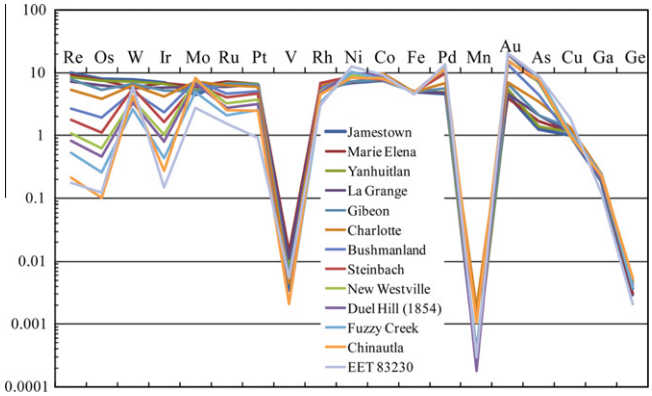

Fig. 5. CI chondrite normalized plot of elemental data for IVA irons and EET 83230 obtained by laser ablation analysis. Elements are arranged from left to right in the order of their 50% condensation temperatures.

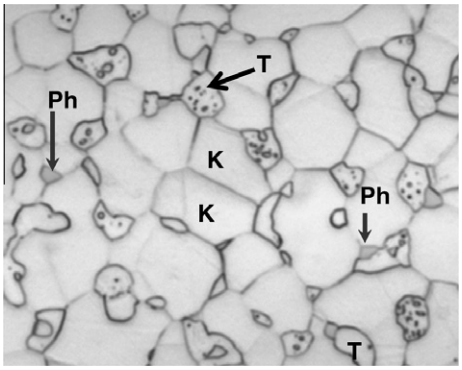

Fig. 6. Reflected light photograph of the Fuzzy Creek microstructure. K, kamacite; T, taenite; and Ph, phosphide. Arrows point to phosphides present at kamacite/kamacite grain boundaries. Field of view is 80 × 70 μm.

bcc martensite and bcc kamacite precipitates. The taenite containing 31–33 wt.% Ni, as measured by the electron microprobe, has a Kurdjumov–Sachs {1 1 0}bcc//{1 1 1}fcc orientation relationship with the adjacent recrystallized kamacite which contains ~7 wt.% Ni.

The taenite regions were observed in more detail in the STEM using thin sections of Fuzzy Creek. Fig. 8a shows a STEM dark field image of a 4 × 4 μm taenite region containing kamacite precipitates. A quantitative X-ray scan showing the Ni and Fe chemical variation in a 1 μm^2 area of the taenite region (Fig. 8a) is shown in Fig. 8b. The taenite–martensite regions have about 25–27 wt.% Ni in their centers (light green) with increasing Ni to >35 wt.% at the interfaces (red) with kamacite, which contains ~7 wt.% Ni (dark blue). Fig. 8c shows a quantitative "M" shaped Ni profile across the taenite in a kamacite/taenite/kamacite region in Fig. 8b.

One cooling rate measurement for Fuzzy Creek was obtained by modeling the nucleation and growth process of a kamacite precipitate which formed inside a taenite grain during slow cooling from the reheating temperature (Fig. 8a–c). We chose the initial composition of the taenite particle as the average taenite composition of 24.5 wt.% Ni for the specific taenite region in Fig. 8a. We assume that P is saturated in taenite, since the bulk P content is 0.18 wt.% and phosphide is prevalent in the meteorite. Therefore, kamacite nucleates by mechanism II ($\gamma \rightarrow \gamma + \text{Ph.} \rightarrow \alpha + \gamma + \text{Ph.}$) according to Yang and Goldstein (2005), and the nucleation temperature for the kamacite precipitates is about 520 °C (793 K) (Yang and Goldstein, 2006). The Fe–Ni and Fe–Ni–P phase diagrams, and the interdiffusion coefficients, which control the growth of the Widmanstätten pattern, are given by Yang et al. (2008). The simulated result using the taenite profile matching method (Goldstein and Ogilvie, 1965) and the measured results (Fig. 8c) match for a given cooling rate at 0.5 K/yr (500,000 K/Myr) (Fig. 8c).

3.4.2. EET 83230

Clarke (1989) described remarkable mm-sized crystals of nearly pure iron phosphate ($Fe_3(PO_4)_2$, sarcopside or graftonite) in EET which are rimmed by troilite. EET has a typical microstructure of an unshocked ataxite, similar to that of an unshocked IVB iron, with precipitates of kamacite within a matrix of plessite (Fig. 9a). No cloudy zone is observed in taenite at high magnification in the SEM, and no apparent post shock or reheating event changes are observed in the microstructure.

The kamacite/taenite interface was observed in more detail using the STEM to determine if a cloudy zone structure is present and if there are any features which indicate a shock or reheating event. Fig. 9b shows a STEM photo of a FIB thin section containing a kamacite plate in a matrix of plessite in EET. The FIB section was cut normal to a kamacite/taenite boundary on the polished surface of the sample. The Ni and Fe chemical variation in a 1 μm^2 area of this microstructure (scan area 1 in Fig. 9b) is shown in Fig. 9c. A Ni composition profile normal to the kamacite/taenite interface is shown in Fig. 9d. The Ni profile is similar

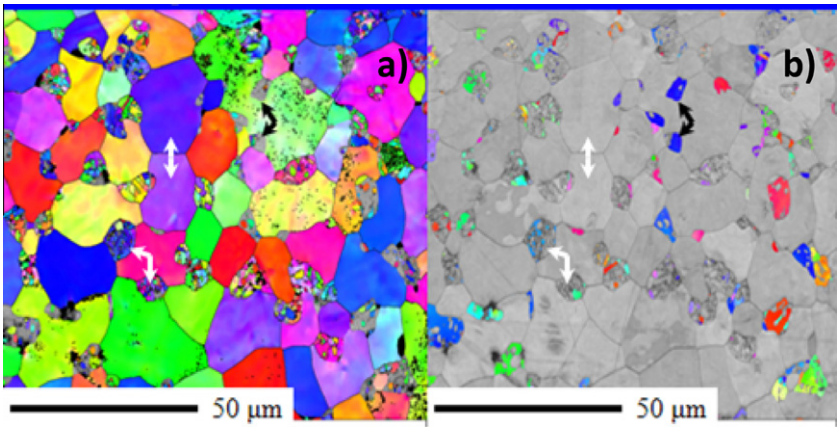

Fig. 7. EBSD analysis of Fuzzy Creek. (a) Bcc polycrystals. Kamacite with ~7 wt.% Ni, fine scale martensite ~24–28 wt.% Ni within Type 2 taenite regions. (b) Fcc poly-crystals ~31–33 wt.% Ni. Curved black arrow points to Type 1 taenite particles formed on kamacite/kamacite boundaries during reheating of the Fuzzy Creek meteorite. Curved white arrow points to Type 2 taenite regions containing residual high Ni taenite (now bcc martensite) from the formation of the Widmanstätten pattern, and high Ni taenite formed at the reheating temperature and during final cooling.

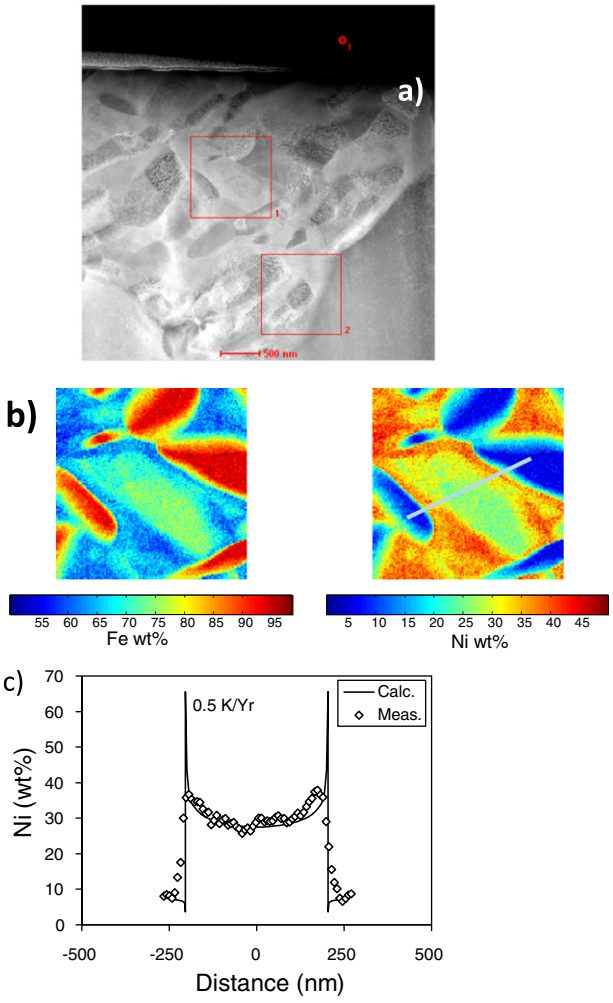

Fig. 8. Detailed microstructure of a Type 2 taenite region in Fuzzy Creek. (a) STEM photo of a 1 × 1 μm region of a Type 2 taenite region at a kamacite grain boundary containing kamacite precipitates. (b) Nickel and Fe chemical variation in a 1 μm^2 area of the microstructure shown in (a). (c) Nickel variation across a kamacite/taenite/kamacite area of a Type 2 taenite region in Fuzzy Creek. The position of the profile is shown in (b). The cooling rate of 0.5 K/yr matches the measured Ni profile.

to that observed for IVB irons with a maximum Ni content at the kamacite/taenite interface of close to 50 wt.% (Yang et al., 2010). There is no evidence from the Ni X-ray scans or Ni composition profiles that EET has been shocked or reheated. In addition, no high-Ni particles or remnants of cloudy zone were observed in this X-ray map or in X-ray maps with an X-ray spatial resolution as small as 2 nm.

A metallographic cooling rate for EET was measured using the taenite profile matching method (Goldstein and Ogilvie, 1965). The bulk P in metal is critical to the cooling rate measurement since the bulk Ni and P content of the metal determines the reaction path to form kamacite and the nucleation temperature. If the phosphate in EET formed after kamacite formed, the P content in the metal was 0.23 wt.% and the kamacite nucleation temperature, according to the Fe–Ni–P phase diagram, was 585 °C (858 K). Cooling rate calculations indicate that there is no match between calculated and measured Ni profiles for a series of possible cooling rates for a nucleation temperature of 585 °C. It is probable that phosphate formed before the cooling temperature reached 585 °C and depleted the P content of the metal. The formation of phosphate will continue to consume some or most of the P in the metal as cooling continues from 585 °C. If all the available P diffuses to phosphate before kamacite forms, the P content will decrease to the solubility limit in kamacite and taenite at low temperatures. We measured a residual of 0.02 wt.% P in the plessite of EET. Assuming that the measured residual P (0.02 wt.%) in the metal was the P content when kamacite formed, the nucleation temperature was ~400 °C (673 K). No match is found for that P content between calculated and measured Ni profiles for a series of possible cooling rates. Therefore, the P content of the metal, when kamacite nucleation occurred, was between 0.23 and 0.02 wt.%. In order to obtain a cooling rate, we assumed that the bulk P was 0.09, 0.07 or 0.05 wt.% P. An excellent match between calculated and measured Ni profiles occurs at a P content of ~0.07 wt.% in the metal. We calculate that the kamacite nucleated at ~475 °C (748 K), and the measured cooling rate is 10,000 ± 3000 K/Myr (Fig. 9d).

4. DISCUSSION

4.1. Cooling histories of Fuzzy Creek and EET 83230

4.1.1. Fuzzy Creek

A meteorite with the bulk chemical composition of Fuzzy Creek (12.4 wt.% Ni and 0.18 wt.% P), would be expected to form a Widmanstätten pattern if the cooling process after crystallization was continuous. However, there is a lack of any microstructural or chemical remnants of a typical IVA Widmanstätten pattern in Fuzzy Creek. Our microstructural observations (optical, SEM, EBSD and STEM) are consistent with the conclusions of Yang et al. (2011) that Fuzzy Creek was heated at temperatures above 650 °C where kamacite was completely converted to taenite and recrystallized so that new taenite grains up to 10 μm in size were formed with diverse orientations. Kamacite formed below 650 °C at taenite grain boundaries and equilibration of kamacite, taenite and phosphide continued until ~510 °C (Yang et al., 2011). Below that temperature, Ni gradients grew and kamacite precipitated in taenite grains below 500 °C.

The "M" shaped Ni profile across the taenite in Fig. 8c is consistent with a process in which cooling below 510 °C took place after the initial reheating which eliminated the initial Widmanstätten microstructure of the meteorite. The Fuzzy Creek cooling rate measurement of 0.5 K/yr (500,000 K/Myr) (Fig. 8c) has a significant error since we were not able to measure the orientation of the kamacite/taenite interface with the direction of the Ni profile, and we were only able to obtain one useful Ni profile due to the lack of other appropriate analysis areas. We estimate the error in this measurement as an order of magnitude, yielding a range of allowable cooling rates from 0.05 to 5 K/yr (5×10^4–5×10^6 K/Myr).

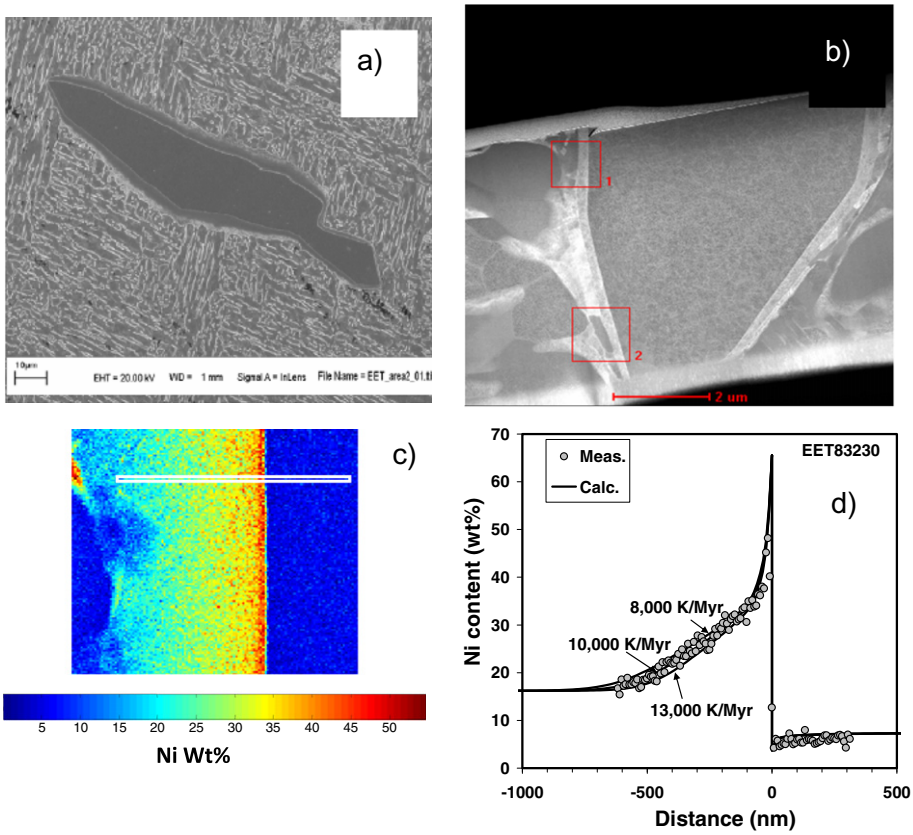

Fig. 9. Microstructure of EET 83230. (a) Microstructure observed by SEM. A kamacite plate is shown in a plessite microstructure. (b) STEM dark field image of a FIB thin section containing a kamacite plate in a matrix of plessite. Two kamacite/taenite interfaces are observed in the section. (c) Nickel and Fe chemical variation in a 1 μm^2 area of region 1 in (b). (d) Nickel profile across the kamacite/taenite interface obtained from the white area in the Ni X-ray area scan of (c). Calculated Ni profiles for cooling rates of 8000, 10,000 and 13,000 K/Myr are plotted across the Ni profile in (d). There is an excellent match with the measured Ni profile yielding a cooling rate of 10,000 K/Myr.

Our investigation of the microstructure of Fuzzy Creek indicates that the meteorite was reheated, probably after Widmanstätten pattern formation, in the core of the IVA parent body. As suggested by Yang et al. (2011), it is plausible that impact reheating occurred during the major impact that shattered the parent IVA metallic body. Such an impact probably occurred soon after the slow cooling of the IVA core.

4.1.2. EET 83230

EET has a typical microstructure of an ataxite, similar to that of a IVB iron, with precipitates of kamacite within a matrix of plessite (Fig. 9a). Unlike irons with an ataxite microstructure, large sized iron phosphates are present in the microstructure, which apparently formed due to higher oxygen fugacity. In addition, unlike unshocked ataxite irons, such as in the IVB chemical group (Goldstein et al., 2009a,b), no cloudy zone is observed in taenite within the resolution limits of the STEM ($<\sim$2 nm).

For low shocked IVA irons at similar cooling rates, high Ni particle sizes of 25 ± 5 nm in the cloudy zone microstructure are measured (Goldstein et al., 2009a,b). No high Ni particles, within the limits of resolution of the STEM ($\sim<$2 nm), were observed in EET. Metallographic cooling rates exceeding 10,000 °C/Myr are deemed necessary for high Ni particle sizes to be smaller than 10 nm (Goldstein et al., 2009a,b). EET has the largest metallographic cooling rate of any unshocked or reheated iron measured to date, $10{,}000 \pm 3000$ °C/Myr (Fig. 9d). Nevertheless, the lack of any cloudy zone microstructure, in a situation with no evidence of shock at the submicroscopic region as observed by STEM, remains to be explained.

The error in the metallographic cooling rate measurement of EET is probably larger than ±30% obtained from the profile matching method, because we were only able to obtain one useful Ni profile due to the lack of other appropriate analysis areas. Nevertheless, the cooling rate of EET is orders of magnitude faster than would be expected if this meteorite formed in the core of the IVA parent body.

4.2. Classification of EET 83230

The analyses of $\Delta^{17}O$ in iron phosphate inclusions in EET lie within the range of values measured for silicates in IVA iron meteorites (Clayton and Mayeda, 1996; Wang et al., 2004). This provides evidence to suggest that EET formed from materials genetically similar to those melted to form the IVA irons. The HSE pattern of EET is also

similar to some in the IVA iron suite, however, the much higher Ni content, coupled with the large difference in cooling rate compared with other evolved IVA irons, probably mean that it did not form from the same magma.

The most likely explanation for these apparently contradictory characteristics is that the meteorite formed in a second parent body. The hit and run impact model of Asphaug et al. (2006) invoked for IVA irons by Ruzicka and Hutson (2006) and Yang et al. (2008), allows for several molten metallic bodies to be formed as part of the same impact onto a larger body, thus, irons from different offspring bodies could have very similar chemical/isotopic compositions, but different cooling histories. For this scenario, EET could have been derived from an independent, much smaller body, having a much faster cooling rate. A similar case for crystallization in genetically related, but distinct parent bodies has previously been made for Fuzzy Creek (Yang et al., 2007), and for Maria Elena (1935), which displays a Widmanstätten pattern when viewed by eye, but has been severely reheated with the formation of rounded taenite regions at kamacite/taenite boundaries. Because of possible minor differences in volatile components, such as S, in secondary metallic bodies, similar, but not necessarily identical crystallization paths would be expected for elements like HSE. Consequently, the good but not perfect fit of the HSE data for EET compared to the IVA irons can be explained.

4.3. ^{187}Re–^{187}Os isotopic constraints

The Re–Os isotopic systematics of the IVA irons define a generally well-constrained isochron. The goodness of fit of the data to a primordial isochron limits possible open-system behavior of Re and Os, and likely the other HSE, to no more than a few tens of Ma subsequent to crystallization. This supports the assumption that the relative HSE abundances of these iron meteorites were set by primary magmatic processes in a core. The initial ^{187}Os/^{188}Os ratio for the isochron is similar to prior estimates for the initial ratio for the solar system (Shen et al., 1996; Smoliar et al., 1996). The Re–Os age of the IVA isochron, within regression uncertainties, is a minimum of 10 Ma younger than the formation of the first solids in the solar system at ~4.567 Ga (e.g., Amelin et al., 2002). A recent U–Pb isotope study of troilites from the IVA iron Muonionalusta, however, reported an older isochron age of 4.5635 ± 0.0005 Ga, indicating crystallization ~3 Ma subsequent to the formation of the first solids in the solar system (Blichert-Toft et al., 2010). The latter age is also consistent with model ^{182}W ages that suggest very early segregation of metal from silicate in the IVA parent body (e.g., Horan et al., 1998; Burkhardt et al., 2009). The disagreement between Re–Os and U–Pb ages of ~0.5% may reflect uncertainties in the ^{187}Re decay constant (not included in the regression uncertainty). However, two independent determinations of the ^{187}Re decay constant differ by only as much as 0.2% (Smoliar et al., 1996; Selby et al., 2007). Selby et al. (2007) based their determination on a cross calibration of Re–Os and U–Pb ages for terrestrial materials. Collectively, these results suggest that uncertainty in the decay constant and cross calibration errors between Re–Os and U–Pb are less than can account for the age differential. The difference in ages may also result from crystallization over an extended period of time, as suggested by the diversity in cooling rates. Muonionalusta likely cooled rapidly, comparable to the cooling rate of similarly evolved Gibeon, whereas some of the most chemically evolved IVA irons with high Re/Os, such as Chinautla may have taken more than 10 Myr to cool sufficiently to become closed to Re–Os transport. Slow cooling of the more evolved portions of the core could lead to generation of a composite IVA isochron with a slightly shallower (younger) slope than would be consistent if all samples crystallized essentially simultaneously.

The only meteorite examined here that plots resolvedly off (below) the IVA isochron is the ungrouped iron EET. We speculate that this reflects minor open-system behavior of Re–Os at least 100 Ma subsequent to crystallization, rather than late crystallization, which would be inconsistent with its rapid cooling rate.

4.4. Crystallization models

Modeling of high precision data for the HSE has proven useful in demonstrating their coherent nature during crystallization of the cores of planetesimals, because of their generally high abundances and predictable relative behaviors resulting from magmatic processes (Pernicka and Wasson, 1987; Chabot, 2004; Petaev and Jacobsen, 2004). A recent HSE study of the IVB magmatic iron meteorites revealed closed-system behavior for the Re–Os isotopic system, and well-behaved differentiation systematics for all of the HSE, given low (<1 wt.%) S and P contents in the parental melt to the IVB system (Walker et al., 2008).

The IVA irons likely began to crystallize from a single, molten mass of iron. Information about the chemical composition of the parent body and the segregated parental metal, as well as the nature of the crystallization process involved (such as liquid–solid mixing) can, therefore, potentially be gleaned via modeling the HSE. In addition to the HSE, the moderately siderophile element (MSE) Ga, another diagnostic trace element, is modeled in order to generate an internally consistent database for IVA irons within the broad sequence of the presumed crystal–liquid fractionation that created them.

Walker et al. (2008) discussed the power of specifically modeling the HSE as a group. Nevertheless, modeling HSE in a dynamic, complex magmatic system can be challenging, given the presence of even small quantities of S and P in iron systems, which reduce the tendency of the liquid to host HSE and MSE. Further, increases in S, and to a lesser extent P, in the liquid are a likely consequence of core crystallization processes, because both are highly incompatible in solid metal. Thus, solid metal–liquid metal D values of most HSE and MSE typically increase as S and P contents increase in the liquid (e.g., Jones and Drake, 1983; Jones and Malvin, 1990; Chabot and Jones, 2003). Modeling of siderophile elements, therefore, requires estimates of the initial S and P content of the system, as well as an understanding of how D values change as crystallization proceeds (Chabot, 2004).

As discussed for modeling the IVB system (Walker et al., 2008), our modeling of the IVA system begins with Re and Os. In brief, this element pair provides a uniquely powerful initial constraint on the chemical composition and processes involved in the formation of iron meteorite systems. This stems from three factors. First, for this study, Re and Os are precisely measured and the ^{187}Re–^{187}Os isotopic systematics of the IVA system requires that abundances of Re and Os have not been modified significantly by processes subsequent to initial crystallization. Second, there is evidence that for this iron group, the initial Re/Os of the IVA iron core was within, or nearly within the range of chondritic meteorites, if it is assumed the parent body had a bulk chondritic composition (see below). Third, because of the linearity of Ir versus Re and Os (as well as Ru and Pt) on logarithmic plots (Fig. 4a), precise, internally consistent relative D values (concentration ratio between solid metal and liquid metal) for Re and Os can be obtained for every increment of crystallization, applying the slopes of those regression lines, coupled with D values for Ir that are appropriate for the S and P content of the liquid modeled and using:

$$\text{Slope of correlation} = [D(\text{HSE}) - 1]/[D(\text{Ir}) - 1] \quad (1)$$

Iridium was the reference element used here for determining absolute D values of Re, Os, Pt and Ru by the slope method, because it is the best experimentally studied of the HSE (see Walker et al. (2008) for further discussion of this approach towards modeling). The D_{Ir} values used here were calculated from the parameterization of Chabot and Jones (2003). Tracking of the compositional evolution of the solid and liquid is done at 0.1% increments of crystallization, along with accounting for the progressive changes in S and P contents of the liquid metal. For all calculations, a constant D value for S of 0.001 was applied. Small changes in D_P, and resulting changes in the concentration of P were calculated using the appropriate S concentration of the liquid and the parameterization for D_P (Chabot and Jones, 2003).

Based on cooling rate considerations, Yang et al. (2008) concluded that early formed IVA irons likely crystallized within the first 10% of fractional crystallization of the IVA parent melt. Consequently, for our modeling, the Re concentration of the hypothesized initial melt was chosen so that the first precipitating solids would have concentrations as similar as possible to that of the least fractionated (highest Re) IVA iron meteorite, Jamestown. The Os concentration was iteratively fitted by adjusting Re/Os to lie within the range of chondritic meteorites (0.082–0.092; Walker et al., 2002). Here we justify the assumption of a chondritic ratio for systems containing lower S (e.g., $\leqslant$3 wt.%), based on a mass balance argument. The least evolved IVA meteorites, such as Jamestown, have relatively high HSE concentrations (e.g., ~380 ng/g Re). If solid metal–liquid metal D_{Re} values for S contents ~3% or lower are applied ($D \leqslant 2.1$), parental melt concentrations necessary to form Jamestown would have to be $\geqslant$190 ng/g. Given that the average Re concentration in chondrites is ~60 ng/g (Walker et al., 2002), this minimum liquid concentration would be consistent with virtually 100% extraction efficiency of HSE into metal in a metal-silicate system in which the metal comprises ~30% of the mass of the system, or >65% extraction efficiency into a core comprising ~20% of the mass of the system. The case becomes stronger for systems with <1 wt.% S where the smaller D values would require high efficiency extraction into a core comprising lower proportions of metal. For higher initial S, this constraint is lifted because of the higher D values and greater possible fractionation of Re/Os in initial precipitates, although the ratio could not have been more than ~10% higher than chondritic, even with 9 wt.% S.

The application of D_{Ir} values calculated for 0.5, 3 and 9 wt.% initial S (and 0.1 wt.% P for each S content), define our Models A, B and C, with initial D values for Re at 1.6, 2.1 and 4.2, respectively, and for Os at 1.7, 2.3 and 4.6, respectively (slope derived D_{Re} values compared to values directly determined using the parameterization of Chabot and Jones (2003) are provided in the Electronic Annex Fig. EA2). One implication of the models is that with higher initial S contents (e.g., $\geqslant$1 wt.%) the higher D values require increasingly lower levels of fractional crystallization to produce most of the diversity of HSE concentrations in the IVA suite. Lower starting S requires considerably more extensive crystal–liquid fractionation to achieve the range of HSE concentrations observed. Models that require limited levels of fractional crystallization become problematic when considering the wide range of cooling rates determined for group IVA.

Model solid and liquid evolution tracks for plots of Re concentration versus Re/Os, together with the data for IVA irons, are shown in Fig. 10a–f. Model A assumes the lowest initial S content, and therefore, is characterized by the lowest D values for Re and Os. This model results in the most limited spread between liquid and solid tracks on plots of Re versus Re/Os. Our model was chosen to have an initial liquid with Re/Os at the high end of the chondritic range (Fig. 10a and b). The Re concentration was chosen to allow formation of Jamestown within the first 2% of crystallization of the body, albeit forming as a 40:60 mixture of initial solid and trapped liquid. For this model it is not possible to use a higher initial Re/Os in the parental melt because increasing the ratio, without decreasing Re, would move the solid and liquid tracks so that Jamestown would plot to the left of the mixing line between the initial melt and solid compositions. For this model, a IVA iron meteorite with an intermediate Re concentration, such as Bushman Land, would be produced after ~80% crystallization. Irons with lower Re would require >80% crystallization. However, our inability to calculate appropriate D values, and the sensitivity of the calculations to D values at such high extents of crystallization precludes meaningful modeling to higher percentages of crystallization. Overall, this model does not fit the IVA data very well. The limited spread between liquid and solid tracks does not allow some of the IVA data to plot between the two tracks, regardless of the starting composition. For example, using Jamestown to constrain the highest initial Re permissible for the suite, several IVA irons with high to moderate Re plot substantially to the right of the solid track. IVA iron compositions in this region of the diagram cannot be achieved by either

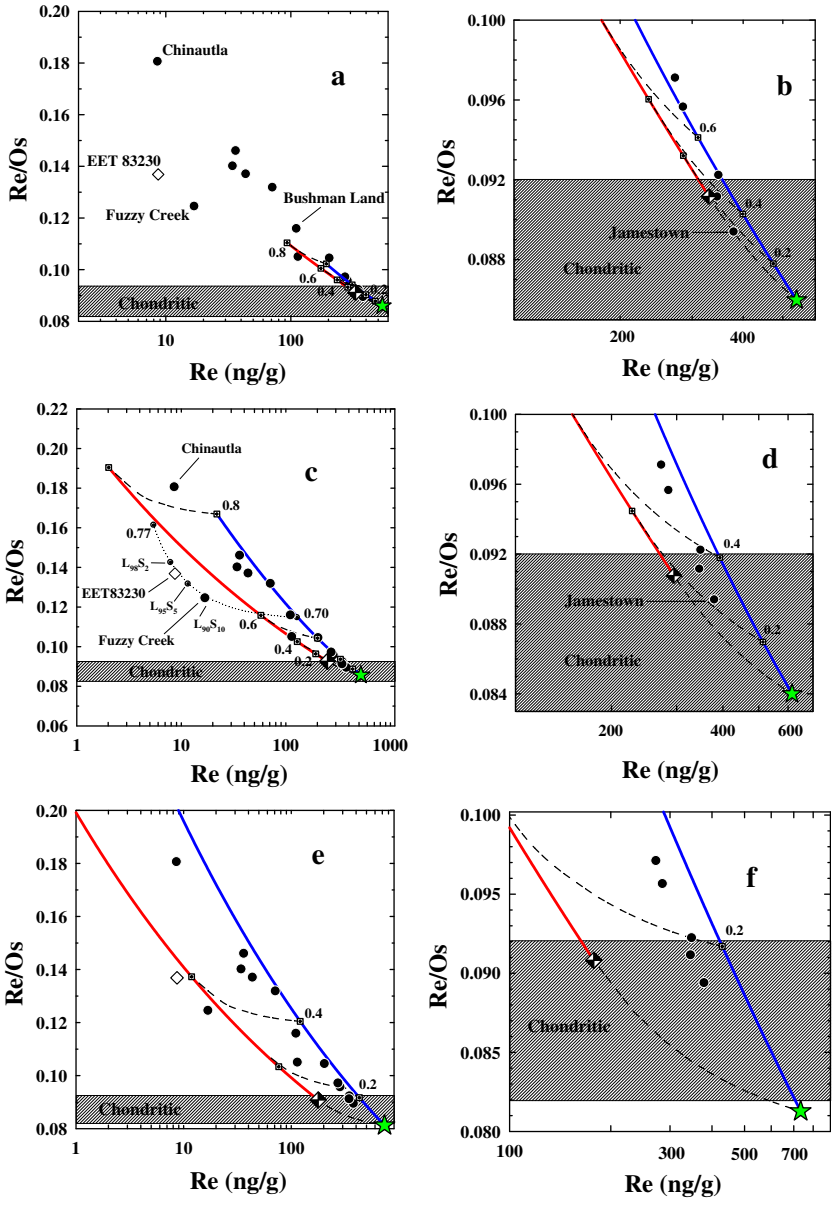

Fig. 10. Fractional crystallization models for Re (in ng/g) versus Re/Os calculated for three sets of starting parameters (Models A, B and C) discussed in the text. Each model is defined by the S and P concentrations assumed for the initial melt. D(Re) and D(Os) were determined relative to D(Ir) via the slope method discussed in the text. The method used to select the initial parameters is also discussed in the text. The black circles are the data for the IVA irons reported by this study. Where duplicate analyses were determined, the symbols shown are averages. Shown for comparison are liquid (red) and solid (blue) evolution tracks, as discussed in the text. The partially filled diamond symbol represents the starting liquid composition. The green star represents the composition of the first solid to form. Open squares with crosses along the liquid and solid tracks correspond to increments of 20% fractional crystallization. Mixing curves (dotted) connect the equilibrium solids and liquids at each of these fractions. The range of Re/Os ratios within which most bulk chondrites plot is shown in the stippled areas. a. Model A with initial S of 0.5 wt.%. (b) Expanded scale view of high Re portion of (a). (c) Model B with initial S of 3 wt.%. (d) expanded scale view of high Re portion of (c). (e) Model C with initial S of 9 wt.%. (f) Expanded scale view of high Re portion of (e). (For interpretation of the references to color in this figure legend, the reader is referred to the web version of this article.)

fractional crystallization or by trapping of liquids in earlier formed solids (see Walker et al. (2008) for details of solid–liquid mixing). Because of this, we discount the possibility of such low initial S.

Model B (Fig. 10c and d) employs a starting liquid composition with Re/Os in the range of chondrites, and Jamestown forming after ~22% crystallization, as approximately a 70:30 mixture of solid and trapped equilibrium liquid. Choosing initial Re and Os concentrations to crystallize Jamestown earlier in the sequence (e.g., after substantially less fractional crystallization), the initial liquid would have to have slightly suprachondritic Re/Os. For example, a starting liquid with Re/Os of ~0.095 and ~200 ng/g Re would be required for Jamestown to form within the first

5% of crystallization. This is plausible given the possibility of modest fractionation of Re/Os during incomplete metal segregation combined with the higher D values accompanying the higher S content. Most other IVA irons examined here fit along either the solid track, or between it and the liquid track. A relatively low Re sample like Duchesne would have formed after >70% fractional crystallization, and Chinautla, with the highest Re/Os of the suite examined, would require >80% fractional crystallization. Fuzzy Creek plots to the left of the liquid track. Its Re–Os elemental systematics could be accounted for only as the result of mixing variable proportions of a highly fractionated liquid (formed after ~80% fractional crystallization) with small proportions of a nearly equally evolved solid (formed after ~70% fractional crystallization) (Fig. 10d). Based solely upon Re–Os data, Model B is judged to be acceptable for the IVA data. Fuzzy Creek shows no petrologic evidence (high abundances of sulfides and/or phosphides) for such high percentages of a liquid component, although that could owe to the small size of these meteorites and unrepresentative sampling. Perhaps some evidence for significant melt trapping in evolved IVA irons comes from Steinbach, which is large enough and fine-grained enough to provide a representative mode. Modal analyses of ~18 cm^2 of Steinbach (Scott et al., 1996) reveals 6.6 vol % troilite, consistent with inclusion of a significant, S-rich trapped melt component.

Model C requires a similarly high amount of fractional crystallization to generate Jamestown in order to maintain the Re/Os of the initial liquid within the range of chondrites. In this case, the Re/Os of the parental melt can be raised as much as 6% above the chondritic range (0.098). The model shown uses a Re/Os at the upper end of the chondritic range for the parental melt (Fig. 10e and f) and is consistent with the formation of Jamestown after ~15% fractional crystallization. The compositions of most other IVA irons are consistent with formation as solids, or mixtures of solids and liquids after anywhere from ~20% to nearly 60% fractional crystallization, with Fuzzy Creek and EET again plotting slightly to the left of the liquid track. As with Model B, their compositions can be accounted for by liquid–solid mixing. Thus, Model C also can successfully account for the Re–Os systematics of the IVA irons.

Given the problems inherent with Model A, only Models B and C are further considered with respect to Pt, Ru, Pd, Au and the volatile siderophile Ga. Table 5 provides initial D values for each element, as well as D values after 80% and 60% fractional crystallization for Models B and C, respectively. Due to their generally similar metal partitioning behavior to Ir, appropriate D values for Pt and Ru were calculated for every increment of crystallization relative to D_{Ir} using Eq. (1) from above. Because of their very different and non-linear behaviors relative to the other HSE, Pd and Au were modeled using D values obtained from the parameterization of Chabot and Jones (2003).

The concentration of Pt was iteratively established next for Models B and C, after Re and Os. Platinum concentrations were chosen to achieve starting melt concentrations with chondritic Pt/Os (between 1.7 and 2.0; Horan et al., 2003), and to match the liquid and solid tracks to the IVA data to be as consistent as possible with the Re–Os portion of the models. The remaining element concentrations were chosen to crystallize solid metal bearing the composition of Jamestown after 15–25% fractional crystallization (where possible), to be consistent with chondritic Re, Os and Pt model results.

Table 5
Bulk distribution coefficients (D values) for modeling fractional crystallization using two models (B and C) discussed in the text.

	B_I	B_{80}	C_I	C_{60}
$Ir_{C\&J}$	1.99	9.95	3.85	51.4
Re	2.09	10.8	4.12	56.3
Os	2.25	12.3	4.61	64.9
Ru	1.43	4.90	2.24	22.9
Pt	1.34	4.07	1.98	18.3
$Pd_{C\&J}$	0.458	0.658	0.531	0.951
$Au_{C\&J}$	0.280	0.541	0.367	1.06
$Ga_{C\&J}$	0.906	2.13	1.29	5.13

I, 80 and 60 subscripts refer to values calculated for the inception of crystallization and after 80% (for Model B) and 60% (for Model C) crystallization. C&J – derived from Chabot and Jones (2003) parameterization. Other values obtained from slopes relative to Ir (Table 3).

Model B and C results for Pt versus Pt/Os are very similar to those of Re versus Re/Os (Fig. 11a–d). For Model B, most IVA meteorite compositions plot between the solid and liquid tracks, with Chinautla requiring ~80% fractional crystallization, similar to Re–Os model results. Fuzzy Creek plots between the liquid and solid tracks, and thus, the relative proportions of solid and liquid estimated by the Re–Os and Pt–Os models are not consistent.

Internally consistent (relative to Re) estimates of the Ir and Ru contents of the parental liquids are iteratively determined for results from Models B and C in plots of Ir versus Re and Ir versus Ru (Electronic Annex Fig. EA3a–d). Both models are consistent with Re–Os and Pt–Os results, but provide little additional discrimination between the initial S contents. Significant differences show up, however, in the amounts of fractional crystallization (i.e., 30–40%) required to generate a lower Ni iron, like Jamestown.

Problems are apparent for Model C in plots of Ir versus Pd, and Ir versus Au (Fig. 12a–d). For both element pairs Model C fails to capture the IVA irons with higher Ni contents between solid and liquid tracks. Thus, unless other factors controlled the behavior of these elements, or the parameterization of Chabot and Jones (2003) is considerably in error, Model C fails to account for the range of compositions present in IVA irons. The success of Model B, compared to Model C, to account for all of the HSE is best illustrated in models of evolution of residual liquids as fractional crystallization progresses (Fig. 13a and b). Model B better describes the Au and Pd variations observed in the IVA suite, compared to Model C.

These findings support a model IVA core with an initial S content of ~3 wt.% (Model B), instead of 0.5 wt.% (Model A) as proposed by Wasson and Richardson (2001) and Wasson et al. (2006), which was based on fitting a quadratic

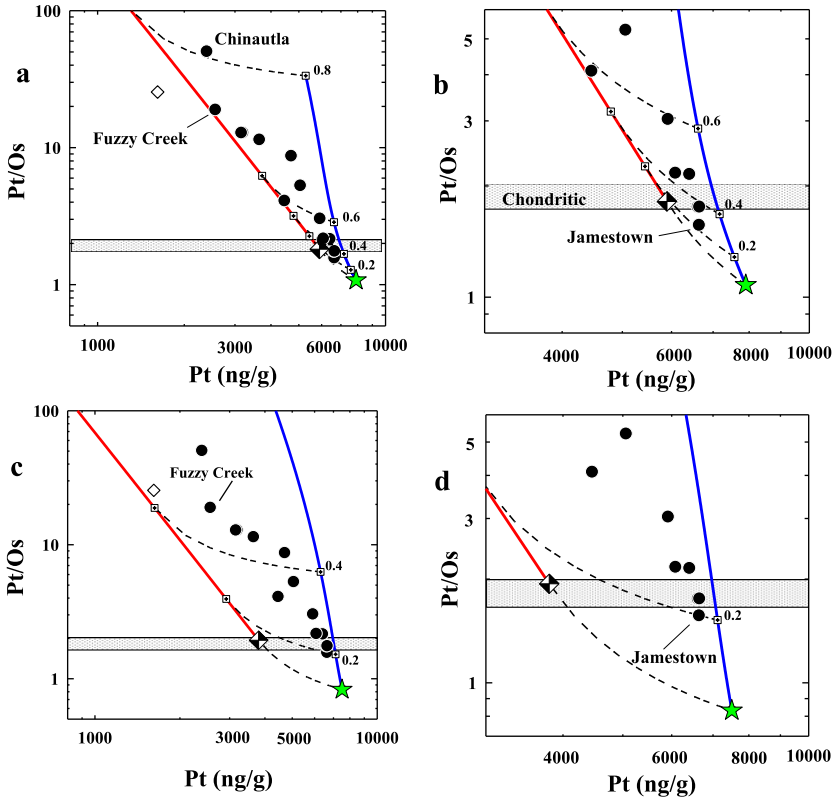

Fig. 11. Fractional crystallization model for Pt (in ng/g) versus Pt/Os calculated for Models B and C discussed in the text. Symbols are the same as for Fig. 10. (a and b) The range of Pt/Os ratios within which most bulk chondrites plot is shown in the stippled areas. (a) Model B with initial S of 3 wt.%. (b) Expanded scale view of high Pt portion of (a). (c) Model C with initial S of 9 wt.%. (d) Expanded scale view of high Pt portion of (c).

equation to Ir–Au and Ir–As, where S was the independent variable. Their fit, however, does not well reproduce experimental data (see Chabot, 2004). Our conclusion of an initial S content of 3 wt.% is in good agreement with studies by Scott et al. (1996) and Chabot (2004), who based their conclusions primarily on Ir–Au correlations, coupled with experimental data.

As noted by previous studies (Scott et al., 1996; Chabot, 2004), the Ir versus Ga trend (or Au versus Ga trend) is more consistent with the higher initial S content of Model C. However, neither model provides a particularly good fit for the data. For Model B (Fig. 14a), many of the IVA data plot outside of the liquid and solid tracks, regardless of the initial melt composition chosen. For Model C, an initial liquid composition can be chosen such that almost all IVA data plot between liquid and solid tracks. Although Model C superficially appears to better account for the IVA Ga data compared to Model B, on close inspection it too inadequately accounts for the changes in concentrations. The HSE define regular, progressive changes in concentrations on element–element plots (Fig. 4a–b). In contrast, early formed IVA irons are characterized by relatively sharp increases in Ga, up to a maximum concentration at Gibeon for our suite. Concentrations then generally decrease slightly with decreasing Ir (Fig. 14a). This observation is not consistent with a gradual change in D_{Ga} as a result of progressive changes in S and P. Such changes in concentrations could occur as a result of an abrupt increase of the solid–liquid D value for Ga that in turn could conceivably result from either the initiation of crystallization of a Ga-rich phase at the point of transition, or a sudden change (increase) in the S content of the liquid. It could also occur as a result of the loss of Ga due to post-crystallization heating of the more evolved IVA irons. None of these options, however, appears to be viable for the IVA system. We are not aware of an appropriate Ga-rich phase whose appearance would lead to an abrupt change in D value. A sudden increase in S content of the melt would likely have an even greater effect on the HSE, which is not observed. Finally, there is considerable evidence that some IVA irons experienced substantial reheating after initial crystallization (e.g., Goldstein et al., 2009a,b). Reheating could possibly lead to volatile loss of Ga, although the reheating temperatures are most likely below 1000 °C, and there is no correlation between the trends and reheating history of the IVA suite. Consequently, we must continue to ascribe changes in Ga to a process that remains unidentified in order to account for its behavior. Although Ge is not discussed here, Ge trends in IVA irons lead to similar reasoning as for Ga.

4.5. IVA core composition and parent body characteristics

Chondrite normalized abundances of refractory through moderately volatile elements (Fig. 5) show effects of at least two distinct processes. First we will consider the refractory

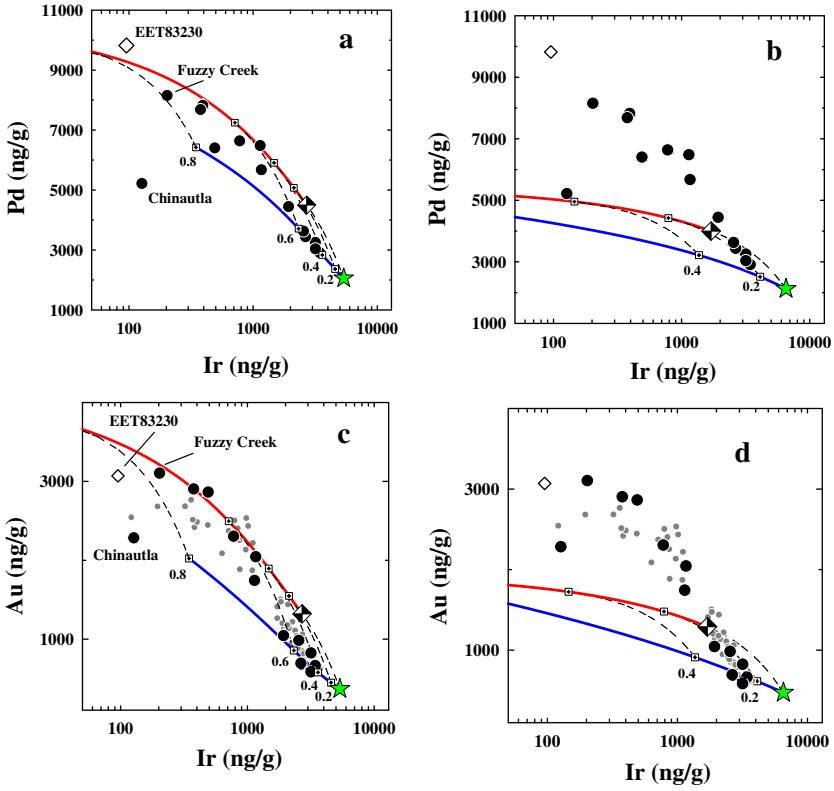

Fig. 12. Fractional crystallization models for Ir versus Pd and Au calculated for Models B and C discussed in the text. Symbols are the same as for Fig. 10. (a) and (c) are for Model B (3 wt.% initial S) and (b) and (d) are for Model C (9 wt.% initial S). Calculations for Pd and Au were made with D values determined using the parameterization method of Chabot and Jones (2003), as discussed in the text. Note that the smaller gray circles represent IVA meteorite data from Wasson and Richardson (2001).

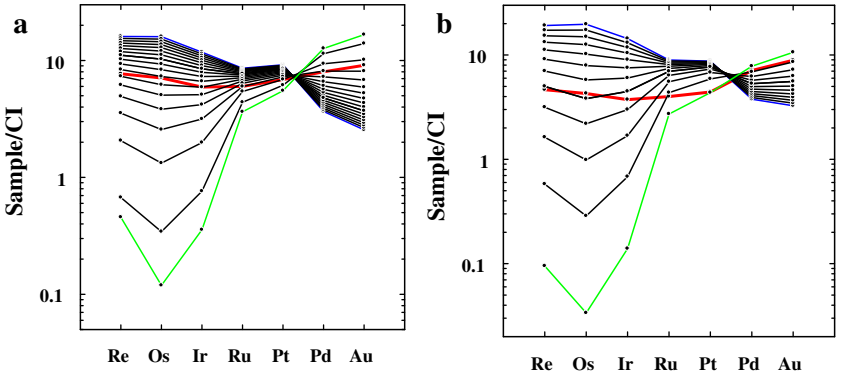

Fig. 13. CI chondrite normalized solid compositions generated via fractional crystallization for every 5 wt.% of crystallization from initial melt compositions shown in red. (a) is for Model B, and (b) is for Model C, as discussed in the text. The blue pattern is the first solid to form and the green pattern is the last to form, after 55 and 85 wt.% crystallization, respectively, for Models B and C. Note that the Model C, with the higher initial S, leads to less variation in the concentrations of Pd and Au than are actually observed for IVA irons (Fig. 3). Note too that Model C requires an HSE pattern for the initial melt that is more fractionated relative to chondritic, than that for Model B. (For interpretation of the references to color in this figure legend, the reader is referred to the web version of this article.)

elements on the left side of Fig. 5. As discussed above, much of the great variance in abundances among some HSE (Re, Os, Ir) can be attributed to, and successfully modeled as the result of solid metal–liquid metal partitioning in the IVA core. Further, our calculated HSE concentrations for the parental melt to the IVA irons (Table 6) are similar to what would be expected for a planetary body with a core that comprises 20–30% of the mass of the body, and that has virtually quantitatively concentrated the HSE from the entire body. For example, the abundances are generally comparable to those proposed for Earth's core (McDonough, 2003; Table 6).

Based on similarities in $\Delta^{17}O$ between IVA silicates and L and LL chondrites (Clayton and Mayeda, 1996), both

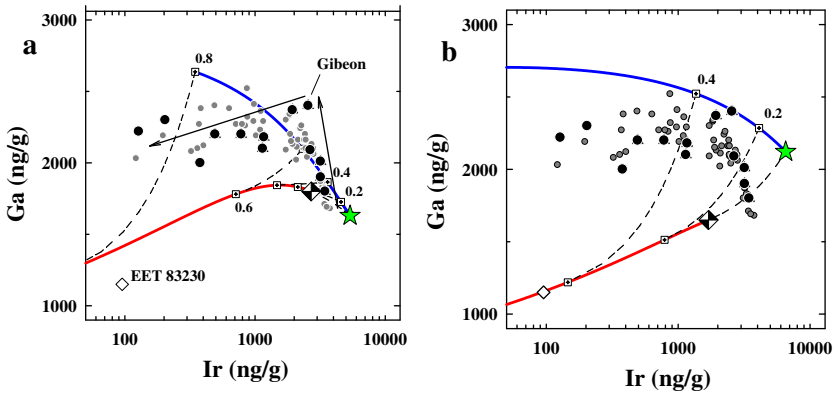

Fig. 14. Fractional crystallization models for Ir versus Ga calculated for Model B (a) and Model C (b). Calculations were made using D values determined using the parameterization method of Chabot and Jones (2003), as discussed in the text. Arrows highlight the two fractionation trends discussed in text. Symbols are the same as in Fig. 10.

Table 6
Calculated initial concentrations for Models B and C discussed in the text (in ng/g). Also provided are estimates for Earth's core, and our model core for an L/LL chondrite-like parent body.

	Re	Os	Ir	Ru	Pt	Pd	Au
Model B	295	3250	2700	3900	5900	4500	1320
Model C	178	1960	1700	2600	3800	4000	1290
Earth	230	2800	2600	4000	5700	3100	500
L/LL core	200	2600	2450	3800	5300	2800	800

Ruzicka and Hutson (2006) and Wasson et al. (2006) developed models for the generation of the IVA parental melt on an L/LL chondrite like parent body, despite some major chemical differences between IVA and L/LL chondrites. With respect to HSE, the IVA parental compositions are broadly similar to the absolute concentrations we calculate for a core that might form in a body with a bulk composition similar to an L or LL chondrite, assuming the mass fraction of the core is 20% of the entire parent body, and using the average L chondrite composition of Wasson and Kallemeyn (1988) for the bulk body (Table 6). In detail, however, the projected IVA core is modestly enriched in the most volatile HSE, Pd and Au, relative to the L chondrite model core (Fig. 15). Thus, the putative HSE compositions for the IVA parental melt are not a very good fit to L/LL-like materials. We do note, however, that because of the greater uncertainties in relative D values for Pd and Au, compared to other HSE in our models, the differences in Pd and Au are not sufficiently compelling to abandon attempts to chemically link IVA with L/LL chondrites.

Based on the compositions of the least differentiated of the IVA irons (Fig. 5) and an assumption of solid metal–liquid metal D values of ~1, the relative abundances of the refractory MSE W, Mo, Fe, Co, Ni are in approximately chondritic relative proportions and at the same level as the HSE. These data are consistent with derivation of the IVA irons from a parent body with largely unfractionated, highly through moderately refractory elements.

The Fe content of the IVA core can be evaluated by comparison to ratios of key siderophile elements in bulk chondrites. The least evolved IVA irons (e.g., Jamestown, Maria Elena (1935) and Yanhuitlan) have values for Fe/Ni of 10, Ni/Co of 19, and Ni/Ir of 4.3×10^4. Average chondritic ratios for Fe/Ni, Ni/Co and Ni/Ir are 17.4 ± 0.5 (1σ), 20.4 ± 0.6 and $2.3(\pm 0.4) \times 10^4$, respectively (Wasson and Kallemeyn, 1988). Thus, as has been noted by prior studies (e.g., Scott et al., 1996) the IVA system is characterized by a moderate depletion in Fe relative to Ni and Co. The depletion in Fe, assuming a planetary body with a chondritic Fe/Ni, requires that the remaining complement of Fe partitioned into the silicate fraction of the body.

The IVA irons also have relatively low P contents, with the least evolved IVA irons having ~0.02 wt.% P (Yang et al., 2008; Goldstein et al., 2009a,b). A low P content for the initial IVA core composition would not be predicted by assuming a chondritic Ni/P ratio (12 ± 2; Wasson and Kallemeyn, 1988). Instead a core with 0.6 wt.% P would be required to be consistent with the Ni content. Assuming the IVA parent body had a chondritic Ni/P, then the IVA core composition with low Fe/Ni and high Ni/P could imply an Fe- and P-depleted core that was (originally) surrounded by a silicate shell with a complementary enrichment in Fe and P. Enrichments in Fe and P in the silicate shell may be achieved via appealing to a relatively oxidized fO_2 accompanying IVA core formation. It is also possible that phosphorous, along with other volatile elements was lost due to volatilization, as might occur during impact (Wasson et al., 2006). This possibility will be considered further below.

It has long been known that the IVA group is depleted in some moderately volatile, siderophile elements, such as Ga and Ge (Schaudy et al., 1972). Models that seek to explain the nature, timing and loss of a volatile component from the IVA body are faced with multiple problems.

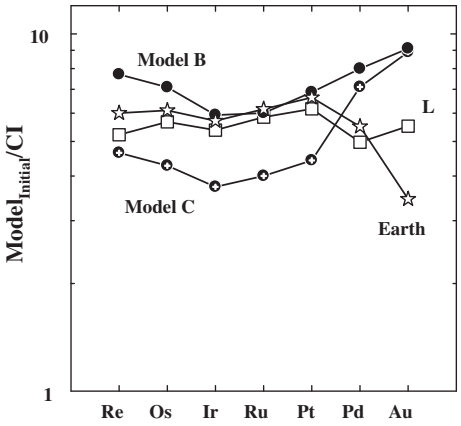

Fig. 15. Plot of calculated initial concentrations of HSE for our Models B and C, normalized to CI chondrites (from Horan et al. (2003) and Anders and Grevesse (1989) for Au) in the parental melt to the IVA core. HSE concentrations for our model L chondrite core (see text), and estimated abundances for Earth's core (McDonough, 2003) are shown for comparison.

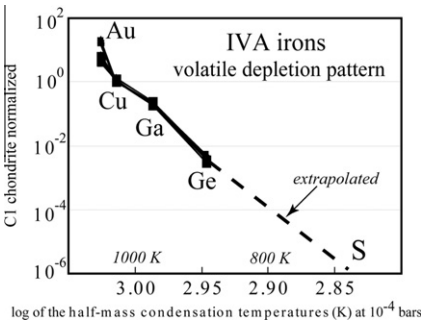

Fig. 16. Chondrite normalized abundance pattern for the moderately volatile elements in the IVA irons versus their 50% mass condensation temperature (Lodders, 2003). With decreasing condensation temperature, the volatile abundances decrease markedly. An extrapolation of the IVA iron data to the much lower condensation temperature for S leads to a prediction that its abundance in the IVA core would be <1 μg/g. This result would be at odds with our modeling of the HSE data. If there is 3 wt.% S in the IVA core, then the depletion trend noted for the moderately volatile elements is only slightly affected by volatile depletion, and instead is mostly due to the partitioning of these elements into the silicate shell of the IVA body.

Chondritic proportions of refractory elements in the IVA core provide a reference frame for the apparent progressive depletion in moderately volatile elements, which appear to follow a depletion trend predicted for a nebular environment (Fig. 16). Notably, in IVA irons Ga is an order of magnitude and Ge is >2 orders of magnitude more depleted than in chondrites. If these elements were wholly extracted into the IVA core, their concentrations would be enriched over a putative parent bulk composition. It is a challenge for any model to explain the Ga and Ge depletions in IVA irons, while also envisaging a IVA core with 3 wt.% S, or even ~0.5 wt.% S, as estimated by Wasson et al. (2006), given that S is a more volatile element. If a conventional nebular depletion model is invoked to explain the Ga and Ge depletions, then a simple extrapolation of this model predicts a volatile depleted core having ~1 ppm S (Fig. 16). Thus, there is an apparent conflict between the Ga–Ge depletion models and a model suggesting the IVA core has between 0.5 and 3 wt.% S.

One way to account for depletions in moderately volatile elements is via loss through impact volatilization. For example, in their model for producing the IVA irons from an L–LL chondrite-like parent, Wasson et al. (2006) argued that metallic Fe was produced from the dissociation of FeO and FeS by impact heating and reduction by C, at or near the surface of the parent body. In addition, Ga and Ge were partially volatilized and lost from the melt at this time. The resulting metallic liquid eventually drained to the center of the body to form a core. Wasson et al. (2006) recognized that the production of metal on a relatively small body via impact heating is a volume limited process. They suggested that the total volume of melting of chondritic material by this process was ~5 km^3. Consequently, they argued for a relatively small parent body (~10–20 km radius) with a small core. If the highly variable cooling rates discussed above are accurate, however, the IVA parent body would have to have been considerably larger, e.g., the ~150 km radius body suggested by Yang et al. (2008). For such a large body the impact melting hypothesis of Wasson et al. (2006) loses viability.

As an alternative to loss through volatilization, we present a model that allows for a IVA core with 3 wt.% S and low Ga and Ge contents. The model is consistent with the prior proposal that the IVA body was assembled from materials having a composition comparable to either an ordinary chondrite (H, L or LL all provide satisfactory fits given existing constraints) with a mild depletion in moderately volatile elements (enough to satisfy the S in the core argument) or an Earth-like composition, given its inventory of moderately depleted volatile elements. Following accretion, the IVA parent body experiences metal-silicate segregation under oxidized conditions, with Ga and Ge partitioned mostly into the silicate shell. The significant constraints for this model are the observation that IVA irons have low Fe/Ni and high Ni/P values relative to chondrites. A prediction of this model is that the silicate shell of the IVA body is enriched in P, Ga and Ge (along with Mn, Cr and V), a composition that is comparable to that predicted by Wasson and Richardson (2001), although they considered that only a minor fraction of Ga and Ge was partitioned into the silicate shell.

The most contentious aspect of this model is the partitioning of Ge between the silicate and metallic phases. There is a significant body of literature demonstrating that Ga can range from lithophile or siderophile depending on the P–T–Xi–fO_2 conditions (Schmidt et al., 1989; Kong and Ebihara, 1996; Capobianco et al., 1999; Jaeger and Drake, 2000; Righter and Drake, 2000; Holzapfel et al., 2001; Liu and Fleet, 2001), but the data for Ge present a less definitive perspective with most findings revealing that it behaves as a siderophile element under most conditions. Experimental investigations reveal that there is a strong bulk compositional dependency on the oxidation states of Ga and Ge in the silicate melts, with Jana and Walker

(1999) observing that under oxidizing conditions Ge becomes less siderophile, and so too Fe, Co, W and P. Core formation on the Earth, which is likely to have occurred under more reducing conditions, resulted in Ga being almost fully lithophile, whereas ~90% of the planetary budget of Ge partitioned into the Earth's core (McDonough, 2003). Overall the marked depletion in Ga and Ge observed in IVA irons may be the result of a combination of factors involving volatilization and oxidation.

5. CONCLUSIONS

(1) New metallographic cooling rates of 500,000 K/Myr and 10,000 ± 3000 K/Myr were determined for Fuzzy Creek and EET 83230, respectively. Chemical and oxygen isotopic evidence indicate a genetic relation between the high Ni EET and group IVA, but the cooling rate for EET is much faster than for any IVA, and especially IVA irons with high Ni. Prior cooling rate data for other IVA irons have led to the suggestion that the IVA group crystallized in a secondary parent body that was deficient in silicate mantle, and formed when a primary parent body was shattered via a large impact. EET most likely crystallized in a smaller secondary parent body that sampled the same core of the primary parent body of the IVA group.

(2) A regression of $^{187}Os/^{188}Os$ versus $^{187}Re/^{188}Os$ data for IVA irons gives an age of 4540 ± 17 Ma. This age is consistent with early solar system formation, and implies that the HSE remained closed systems after initial crystallization.

(3) We have modeled fractional crystallization using new highly siderophile element data, assuming initial S abundances of 0.5, 3 and 9 wt.%. Given our assumed initial elemental ratios and *D* values, our attempts to model Re and Os abundances resulting from fractional crystallization of a melt with 0.5 wt.% S were unsuccessful, suggesting that higher S concentrations were present in the initial IVA proto-body melt. Models employing either 3 or 9 wt.% S can explain Re, Os, Pt and Ru abundances, while only 3 wt.% S initial melts can successfully be used to model Pd and Au. Abundances of the volatile siderophile Ga cannot be adequately modeled at either S concentration, suggesting that some as yet unidentified mechanism is needed to account for its behavior.

(4) The overall depletion in Fe, P, Ga and Ge in IVA irons may result from sequestration of these elements into the mantle of the primary parent body during differentiation under relatively oxidizing conditions, or volatilization or some combination of these.

ACKNOWLEDGMENTS

Funding for this work was provided by NASA Grants NNG06GF56G (to T.J.M.), NNX07AM29G and NNX10AG94G (to R.J.W.), NNX08AG53G (to J.I.G.), NNX09AG90G (to N.L.C.) and NNX08AH76G (to W.F.M.) which is gratefully acknowledged. The authors thank Janne Blichert-Toft for the sample of Muonionalusta.

APPENDIX A. SUPPLEMENTARY DATA

Supplementary data associated with this article can be found, in the online version, at doi:10.1016/j.gca.2011.09.006.

REFERENCES

Achterbergh E. V., Ryan C. G., Jackson S. E. and Griffin W. L. (2001) Appendix 3: data reduction software for LA-ICP-MS. In *Laser Ablation-ICP-MS in the Earth Sciences*, vol. 29 (ed. P. Sylvester). *Mineralogical Association of Canada, Short Course Series*, 243pp.

Amelin Y., Krot A. N., Hutcheon I. D. and Ulyanov A. A. (2002) Lead isotopic ages of chondrules and calcium–aluminum rich inclusions. *Science* **297**, 1678–1683.

Anders E. and Grevesse N. (1989) Abundances of the elements: meteoritic and solar. *Geochim. Cosmochim. Acta* **53**, 197–214.

Asphaug E., Agnor C. B. and Williams Q. (2006) Hit-and-run planetary collisions. *Nature* **439**, 155–160.

Asprey L. B. (1976) The preparation of very pure fluorine gas. *J. Fluorine Chem.* **7**, 359–361.

Becker H., Horan M. F., Walker R. J., Gao S., Lorand J.-P. and Rudnick R. L. (2006) Highly siderophile element composition of the Earth's primitive upper mantle: constraints on new data on peridotite massifs and xenoliths. *Geochim. Cosmochim. Acta* **70**, 4528–4550.

Birck J.-L., Roy-Barman M. and Capmas F. (1997) Re–Os isotopic measurements at the femtomole level in natural samples. *Geostand. Newsl.* **20**, 9–27.

Blichert-Toft J., Moynier F., Lee C.-T., Telouk P. and Albarede F. (2010) The early formation of the IVA iron meteorite parent body. *Earth Planet. Sci. Lett.* **296**, 469–480.

Buchwald V. F. (1975) *Handbook of Iron Meteorites*. University of California Press, Berkeley, CA.

Burkhardt C., Kleine T., Bourdon B., Palme H., Zipfel J., Friedrich J. and Ebel D. (2009) Hf–W mineral isochron for Ca, Al rich inclusions: age of the solar system and the timing of core formation in planetesimals. *Geochim. Cosmochim. Acta* **72**, 6177–6197.

Capobianco C. J., Drake M. J. and De'Aro J. (1999) Siderophile geochemistry of Ga, Ge, and Sn: cationic oxidation states in silicate melts and the effect of composition in iron–nickel alloys. *Geochim. Cosmochim. Acta* **63**, 2667–2677.

Chabot N. L. (2004) Sulfur contents of the parental metallic cores of magmatic iron meteorites. *Geochim. Cosmochim. Acta* **68**, 3607–3618.

Chabot N. L. and Jones J. H. (2003) The parameterization of solid metal–liquid metal partitioning of siderophile elements. *Meteorit. Planet. Sci.* **38**, 1425–1436.

Clarke R. S. (1989) Description of some Antarctic iron meteorites. *Smithsonian Contrib. Earth Sci.* **28**, 61–63.

Clayton R. N. and Mayeda T. K. (1996) Oxygen isotope studies of achondrites. *Geochim. Cosmochim. Acta* **60**, 1999–2017.

Cliff G. and Lorimer G. W. (1975) The quantitative analysis of thin specimens. *J. Microsc.* **103**, 203–207.

Cohen A. S. and Waters F. J. (1996) Separation of osmium from geological materials by solvent extraction for analysis by thermal ionisation mass spectrometry. *Anal. Chim. Acta* **332**, 269–275.

Cook D. L., Walker R. J., Horan M. F., Wasson J. T. and Morgan J. W. (2004) Pt–Re–Os systematics of group IIAB and IIIAB iron meteorites. *Geochim. Cosmochim. Acta* **68**, 1413–1431.

Cook D. L., Wadhwa M., Clayton R. N., Janney P. E., Dauphas N. and Davis A. M. (2005) Nickel isotopic composition of Fe–Ni metal from iron meteorites and the Brenham pallasite. *Lunar Planet. Sci. Conf.* (CD-ROM) **36**, #1836.

Creaser R. A., Chen J. H., Papanastassiou D. A. and Wasserburg G. J. (1991) Isotopic analysis of osmium, rhenium, and iridium by negative thermal ion mass spectrometry. *Lunar Planet. Sci. Conf.* **XXII**, 255–256.

Goldstein J. I. and Ogilvie R. E. (1965) The growth of the Widmanstätten pattern in metallic meteorites. *Geochim. Cosmochim. Acta* **29**, 893–920.

Goldstein J. I. and Short J. M. (1967) The iron meteorites, their thermal history and parent bodies. *Geochim. Cosmochim. Acta* **31**, 1733–1770.

Goldstein J. I., Scott E. R. D. and Chabot N. L. (2009a) Iron meteorites: crystallization, thermal history, parent bodies, and origin. *Chem. Erde* **69**, 293–325.

Goldstein J. I., Yang J., Kotula P. G., Michael J. R. and Scott E. R. D. (2009b) Thermal histories of IVA iron meteorites from transmission electron microscopy of the cloudy zone microstructure. *Meteorit. Planet. Sci.* **44**, 343–358.

Haack H., Scott E. R. D., Love S. G., Brearley A. J. and McCoy T. J. (1996) Thermal histories of IVA stony-iron and iron meteorites: evidence for asteroid fragmentation and reaccretion. *Geochim. Cosmochim. Acta* **60**, 3103–3113.

Hamester M., Wiederin D., Wills J., Kerl W. and Douthitt C. B. (1999) Strategies for isotope ratio measurements with a double focusing sector field ICP-MS. *Fresenius J. Anal. Chem.* **364**, 495–497.

Holzapfel C., Courtial P., Dingwell D. B., Chakraborty S. and Palme H. (2001) Experimental determination of partial molar volumes of Ga_2O_3 and GeO_2 in silicate melts: implications for the pressure dependence of metal–silicate partition coefficients. *Chem. Geol.* **174**, 33–49.

Horan M. F., Morgan J. W., Walker R. J. and Grossman J. N. (1992) Rhenium–osmium isotope constraints on the age of iron meteorites. *Science* **255**, 1118–1121.

Horan M. F., Smoliar M. I. and Walker R. J. (1998) ^{182}W and ^{187}Re–^{187}Os systematics of iron meteorites: chronology for melting, differentiation, and crystallization in asteroids. *Geochim. Cosmochim. Acta* **62**, 545–554.

Horan M. F., Walker R. J., Morgan J. W., Grossman J. N. and Rubin A. (2003) Highly siderophile elements in chondrites. *Chem. Geol.* **196**, 5–20.

Jaeger W. L. and Drake M. J. (2000) Metal–silicate partitioning of Co, Ga, and W: dependence on silicate melt composition. *Geochim. Cosmochim. Acta* **64**, 3887–3895.

Jana D. and Walker D. (1999) Core formation in the presence of various C–H–O volatile species. *Geochim. Cosmochim. Acta* **63**, 2299–2310.

Jones J. H. and Drake M. J. (1983) Experimental investigations of trace element fractionation in iron meteorites, II: the influence of sulfur. *Geochim. Cosmochim. Acta* **47**, 1199–1209.

Jones J. H. and Malvin D. J. (1990) A nonmetal interaction model for the segregation of trace elements during solidification of Fe–Ni–S, Fe–Ni–P, and Fe–Ni–S–P alloys. *Metall. Trans. B* **21B**, 697–706.

Jones A. M., Iacumin P. and Young E. D. (1999) High-resolution $\delta^{18}O$ analysis of tooth enamel phosphate by isotope ratio monitoring gas chromatography mass spectrometry and ultraviolet laser fluorination. *Chem. Geol.* **153**, 241–248.

Kong P. and Ebihara M. (1996) Metal phases of L chondrites: their formation and evolution in the nebula and in the parent body. *Geochim. Cosmochim. Acta* **60**, 2667–2680.

Lodders K. (2003) Solar System abundances and condensation temperatures of the elements. *Astrophys. J.* **591**, 1220–1247.

Luck J.-M., Birck J.-L. and Allegre C.-J. (1980) Re-187/Os-187 systematics in meteorites – early chronology of the solar system and age of the Galaxy. *Nature* **283**, 256–259.

Ludwig K. R. (2003) Isoplot 3.00. Berkeley Geochronology Center, Special Publication No. 4, 70pp.

Liu M. and Fleet M. E. (2001) Partitioning of siderophile elements (W, Mo, As, Ag, Ge, Ga, and Sn) and Si in the Fe–S system and their fractionation in iron meteorites. *Geochim. Cosmochim. Acta* **65**, 671–682.

McDonough W. F. (2003) Compositional model for the Earth's core. In *The Mantle and Core*, vol. 2 (ed. R. W. Carlson) (eds. H. D. Holland and K. K. Turekian). Elsevier-Pergamon, Oxford, pp. 547–568.

Pernicka E. and Wasson J. T. (1987) Ru, Re, Os, Pt and Au in iron meteorites. *Geochim. Cosmochim. Acta* **51**, 1717–1726.

Petaev M. I. and Jacobsen S. B. (2004) Differentiation of metal-rich meteorite parent bodies: I. Measurements of PGEs, Re, Mo, W, and Au in meteoritic Fe–Ni metal. *Meteorit. Planet. Sci.* **39**, 1685–1697.

Rasmussen K. L., Ulff-Moller F. and Haack H. (1995) The thermal evolution of IVA iron meteorites: evidence from metallographic cooling rates. *Geochim. Cosmochim. Acta* **59**, 3049–3059.

Rehkämper M., Halliday A. N., Barfod D., Godfrey F. J. and Dawson B. J. (1997) Platinum-group element abundance patterns in different mantle environments. *Science* **278**, 1595.

Righter K. and Drake M. J. (2000) Metal/silicate equilibrium in the early Earth – new constraints from the volatile moderately siderophile elements Ga, Cu, P, and Sn. *Geochim. Cosmochim. Acta* **64**, 3581–3597.

Rumble D., Farquhar J., Young E. D. and Christensen C. P. (1997) *In situ* oxygen isotope analysis with an excimer laser using F_2 and BrF_5 reagents and O_2 gas as analyte. *Geochim. Cosmochim. Acta* **61**, 4229–4234.

Rumble, III, D., Miller M. F., Franchi I. A. and Greenwood R. C. (2007) Oxygen three-isotope fractionation lines in terrestrial silicate minerals: an inter-laboratory comparison of hydrothermal quartz and eclogitic garnet. *Geochim. Cosmochim. Acta* **71**, 3592–3600.

Ruzicka A. and Hutson M. (2006) Differentiation and evolution of the IVA meteorite parent body: clues from pyroxene geochemistry in the Steinbach stony-iron meteorite. *Meteorit. Planet. Sci.* **41**, 1959–1987.

Schaudy R., Wasson J. T. and Buchwald V. F. (1972) The chemical classification of iron meteorites. VI. A reinvestigation of irons with Ge concentrations lower than 1 ppm. *Icarus* **17**, 174–192.

Schmidt W., Palme H. and Wänke H. (1989) Experimental determination of metal/silicate partition coefficients for P, Co, Ni, Cu, Ga, Ge, Mo, and W and some implications for the early evolution of the Earth. *Geochim. Cosmochim. Acta* **53**, 173–185.

Scott E. R. D. (1972) Chemical fractionation in iron meteorites and its interpretation. *Geochim. Cosmochim. Acta* **36**, 1205–1236.

Scott E. R. D., Haack H. and McCoy T. J. (1996) Core crystallization and silicate–metal mixing in the parent body of the IVA iron and stony-iron meteorites. *Geochim. Cosmochim. Acta* **60**, 1615–1631.

Sears D. W. (1978) Condensation and the composition of iron meteorites. *Earth Planet. Sci. Lett.* **41**, 128–138.

Selby D., Creaser R. A., Stein H. J., Markey R. J. and Hannah J. L. (2007) Assessment of the ^{187}Re decay constant by cross calibration of Re–Os molybdenite and U–Pb zircon chronom-

eters in magmatic ore systems. *Geochim. Cosmochim. Acta* **71**, 1999–2013.

Shen J. J., Papanastassiou D. A. and Wasserburg G. J. (1996) Precise Re–Os determinations and systematic of iron meteorites. *Geochim. Cosmochim. Acta* **60**, 2887–2900.

Shirey S. B. and Walker R. J. (1998) The Re–Os isotope system in cosmochemistry and high-temperature geochemistry. *Ann. Rev. Earth Planet. Sci.* **26**, 423–500.

Smoliar M. I., Walker R. J. and Morgan J. W. (1996) Re–Os ages of group IIA, IIIA, IVA, and IVB iron meteorites. *Science* **271**, 1099–1102.

Walker R. J., Horan M. F., Morgan J. W., Becker H., Grossman J. N. and Rubin A. E. (2002) Comparative ^{187}Re–^{187}Os systematic of chondrites – implications regarding early solar system processes. *Geochim. Cosmochim. Acta* **66**, 4187–4201.

Walker R. J., McDonough W. F., Honesto J., Chabot N. L., McCoy T. J., Ash R. D. and Bellucci J. J. (2008) Modeling fractional crystallization of Group IVB iron meteorites. *Geochim. Cosmochim. Acta* **72**, 2198–2216.

Wang P.-L., Rumble D. and McCoy T. J. (2004) Oxygen isotopic compositions of IVA iron meteorites: implications for the thermal evolution derived from in situ ultraviolet laser microprobe analyses. *Geochim. Cosmochim. Acta* **68**, 1159–1171.

Wasson J. T. (1999) Trapped melt in IIIAB irons: solid/liquid elemental partitioning during the fractionation of the IIIAB magma. *Geochim. Cosmochim. Acta* **63**, 2875–2889.

Wasson J. T. and Kallemeyn G. W. (1988) Compositions of chondrites. *Philos. Trans. R. Soc. Lond. Ser. A* **325**(1587), 535–544, The Solar System: Chemistry as a Key to its Origin (Jul. 29, 1988).

Wasson J. T. and Richardson J. W. (2001) Fractionation trends among IVA iron meteorites: contrasts with IIIAB trends. *Geochim. Cosmochim. Acta* **65**, 951–970.

Wasson J. T., Matsunami Y. and Rubin A. E. (2006) Silica and pyroxene in IVA irons; possible formation of the IVA magma by impact melting and reduction of L–LL-chondrite materials followed by crystallization and cooling. *Geochim. Cosmochim. Acta* **70**, 3149–3172.

Wiechert U. and Hoefs J. (1995) An excimer laser-based micro analytical preparation technique for in-situ oxygen isotope analysis of silicate and oxide minerals. *Geochim. Cosmochim. Acta* **59**, 4093–4101.

Willis J. and Goldstein J. I. (1982) The effects of C, P, and S on trace element partitioning during solidification in Fe–Ni alloys. In *Proc. Lunar Planet. Sci. Conf., 13th, Part I. J. Geophys. Res.* **87** (Suppl.) A435–A445.

Yang J. and Goldstein J. I. (2005) The formation mechanism of the Widmanstätten structure in meteorites. *Meteorit. Planet. Sci.* **40**, 239–253.

Yang J. and Goldstein J. I. (2006) Metallographic cooling rates of the IIIAB iron meteorites. *Geochim. Cosmochim. Acta* **70**, 3197–3215.

Yang J., Goldstein J. I. and Scott E. R. D. (2007) Iron meteorite evidence for early formation and catastrophic disruption of protoplanets. *Nature* **446**, 888–891.

Yang J., Goldstein J. I. and Scott E. R. D. (2008) Metallographic cooling rates of the IVA iron meteorites. *Geochim. Cosmochim. Acta* **72**, 3043–3061.

Yang J., Goldstein J. I., Michael J. R., Kotula P. G. and Scott E. R. D. (2010) Thermal history and origin of the IVB iron meteorites and their parent body. *Geochim. Cosmochim. Acta* **74**, 4493–4506.

Yang J., Goldstein J. I., Scott E. R. D., Michael J. R., Kotula P. G., Pham T. and McCoy T. J. (2011) Thermal and impact histories of reheated group IVA, IVB and ungrouped iron meteorites and their parent asteroids. *Meteorit. Planet. Sci.* **46**, 1227–1252.

Associate editor: Alexander N. Krot